THESIS FOR THE DEGREE OF LICENTIATE OF PHILOSOPHY

Self-Trapped Excitons in Bismuth Vanadate: A Play of Counterparts

Tobias Möslinger

Department of Physics and Astronomy
CHALMERS UNIVERSITY OF TECHNOLOGY
Göteborg, Sweden 2026

Self-Trapped Excitons in Bismuth Vanadate:
A Play of Counterparts
Tobias Möslinger

Department of Physics and Astronomy
Chalmers University of Technology
se-412 96 Göteborg, Sweden
Telephone +46 (0)31 772 10 00

Cover: A closer look into bismuth vanadate. Glowing turquoise and pink charge isosurfaces show the structure of a self-trapped exciton (electron-hole pair).

Chalmers digitaltryck
Göteborg, Sweden 2026

Self-Trapped Excitons in Bismuth Vanadate: A Play of Counterparts

Tobias Möslinger
Department of Physics and Astronomy
Chalmers University of Technology

Abstract

Climate change and the persistent dominance of fossil fuels in global energy systems highlight the urgent need for sustainable alternatives. Hydrogen, produced via photoelectrochemical (PEC) water splitting, offers a green energy carrier. However, the efficiency of the PEC process is generally limited by charge carrier dynamics in photoanode materials. Bismuth vanadate ($BiVO_4$), a potential material for PEC water splitting, is particularly prone to charge localization in the form of small polarons and self-trapped excitons (STEs), which can potentially affect its performance. While the formation of polarons in $BiVO_4$ has been widely studied, the precise nature, stability, and behaviour of STEs, especially under operating conditions, remain poorly understood. In this thesis, these gaps are addressed using advanced computational methods. First, time-dependent density functional theory (TD-DFT) with hybrid functionals is employed to investigate the localization, stability, and optical properties of STEs in $BiVO_4$. The results reveal two distinct localized exciton configurations: one separated, more mobile state, and one compact, more rigid state, with comparable energies. Second, hybrid density functional theory (DFT) combined with the nudged elastic band (NEB) method is used to quantify activation barriers for STE hopping, dissociation, and transformation. This analysis reveals distinct kinetic behaviours for the two STE types, where the separated, more mobile state exhibits much lower barriers than the compact, more rigid state. Additionally, an alternative charge-trapping mechanism involving O–O hole dimers is explored, providing insights into a multipolaron binding pathway with much slower kinetics compared to STEs.

Keywords: bismuth vanadate, density functional theory, electronic structure theory, nudged elastic band, polaron, self-trapped exciton, semiconductor, solar energy, water splitting

LIST OF APPENDED PAPERS

This thesis consists of an introductory text and the following papers:

I **Competing Self-Trapped Exciton States and Multiple Emission Pathways in $BiVO_4$**
Tobias Möslinger, Nicklas Österbacka, and Julia Wiktor
The Journal of Physical Chemistry Letters **16**, 6861-6865 (2025)

II **Evolution of Excited States in Bismuth Vanadate: Trapping and Kinetic Pathways**
Tobias Möslinger and Julia Wiktor
The Journal of Physical Chemistry Letters **17**, 5646-5651 (2026)

The author's contribution to the papers:

I I performed the calculations and analysis of results concerning self-trapped exciton formation and emission energies and stability, prepared the corresponding figures and assisted with writing the related sections of the paper.

II I performed the calculations and analysis of results, prepared the figures and wrote the first draft of the paper, which was finalized together with the co-author.

PUBLICATIONS NOT INCLUDED IN THIS THESIS

The following publications are outside the scope of this thesis:

Reaction Kinetics of Liquid Organic Hydrogen Carriers from First-Principles: The Methylcyclohexane/Toluene Pair on Pt(111)
Alvaro Posada-Borbón, **Tobias Möslinger**, and Henrik Grönbeck
ACS Catalysis **16**, 12123–12134 (2026)

Stability of Polarons and Oxygen Vacancies in $BiVO_4$ Revealed by Machine-Learning-Driven Simulations
Ethan Berger, Tobias Hainer, **Tobias Möslinger**, Paul Erhart, and Julia Wiktor
PRX Energy **5**, 033004 (2026)

Contents

List of Abbreviations

ADMM auxiliary density matrix method.

$BiVO_4$ bismuth vanadate.
BSE Bethe–Salpeter equation.

CBM conduction band minimum.
CI climbing image.

DFT density functional theory.

FFT fast Fourier transform.

GGA generalized gradient approximation.
GW+BSE GW approximation and BSE.

HER hydrogen evolution reaction.

LDA local density approximation.

ms monoclinic scheelite.

NEB nudged elastic band.

OER oxygen evolution reaction.

PAW projector augmented waves.
PBE Perdew, Burke, and Ernzerhof.
PEC photoelectrochemical.
ppb parts per billion.
ppm parts per million.

SHE standard hydrogen electrode.
STE self-trapped exciton.

TD-DFT time-dependent density functional theory.
ts tetragonal scheelite.

UV ultraviolet.

VASP Vienna Ab initio Simulation Package.
VBM valence band maximum.

1

The Challenge: Introduction

In today's world, anthropogenic carbon (CO_2) emissions are at a level of about 40 Gt per year, causing a CO_2 concentration of around 430 parts per million (ppm) in the atmosphere. This is, with high confidence, higher than at any time during, at least, the past two million years. The increase in CO_2 concentration is 54 % since 1750. However, CO_2 is not the only greenhouse gas whose atmospheric abundance has increased. Methane (CH_4), for example, has reached 1940 parts per billion (ppb), a rise of 169 % since 1750 [1–3].

Fossil fuels and industry account for approximately 85 % of annual CO_2 emissions, with the remaining 15 % originating from land use and forestry. As CO_2 is the largest driver of global warming, immediate and drastic emission reductions are required to still have a chance of staying below the global warming limit of 1.5 °C (or even 2 °C), reaching net-zero in 25 to 45 years [1].

Sustainable solutions to replace traditional fossil energy sources, which drive climate change, increase air pollution, and, in addition, contribute to geopolitical tensions, have been developed and implemented in some areas of application. However, while many options have been explored and found to be practical, the share of renewable energies worldwide is still only around 15 % [4]. One reason for this low percentage is challenges regarding availability, storage, and transport. The use of renewable energy is typically dependent on location (for example rivers, areas with sufficient wind or sunlight) and time (like seasons or daytime), which do not always correspond to the needs of the society. Therefore, additional long-term storage possibilities as well as efficient transportation options are required to balance supply and demand. Batteries are one way to store energy, and current research is being carried out to develop improved technologies that, on the one hand, can store larger amounts of electric energy and, on the other hand, require fewer rare natural resources and therefore pose a lower environmental impact and cost. However, alternative solutions to batteries are also investigated.

A promising candidate as an energy carrier is hydrogen, which can easily be converted into electrical energy in fuel cells, emitting only water as a by-product. Liquid hydrogen has an energy density of 2.4 kWh/L or a specific energy of 33 kWh/kg. Compared to a fossil fuel like gasoline with 9.5 kWh/L, but only 12 kWh/kg, hydrogen can store nearly three times more energy per unit mass [5]. Beyond its role as an energy carrier, hydrogen is also a key component in the chemical industry, where it is used for the production of a wide range of chemicals. This versatility enables applications for energy storage (for example seasonal storage and peak relief for grids), in industrial processes where high energies are required (for example steel or ammonia production), and as a decarbonization pathway in sectors that are difficult to electrify (for example remote or hard-to-reach areas, shipping, aviation, or heavy industry). Nevertheless, there are some challenges that limit the application of hydrogen at the moment. One of those is that although hydrogen can be obtained by water splitting in a climate-friendly way using renewable energies (green hydrogen), around 95 % of hydrogen worldwide is still produced from fossil fuels (grey hydrogen) [6]. The main reasons for this are the high electricity demand for a sustainable process as well as the inefficiency of alternative methods.

In this thesis, current water splitting processes and promising future solutions are discussed in Chapter 2 and Chapter 3. Important electronic phenomena that could influence the properties of photoactive materials, such as polarons and self-trapped excitons (STEs), are discussed in Chapter 5 and analyzed according to the techniques introduced in Chapter 4. Finally, the papers on which the thesis is based are presented in Chapter 6, and future research directions are outlined in Chapter 7.

2

The Process: Water Splitting

2.1 The Need for Green Hydrogen

The production of hydrogen can be achieved via water splitting, where water molecules are separated into molecular hydrogen and oxygen using renewable energy sources like solar, wind, or hydropower. This enables a potentially carbon-neutral pathway that delivers green hydrogen without direct CO_2 emissions during operation. It therefore offers significant advantages over grey hydrogen (produced from fossil fuels) or blue hydrogen (fossil fuels and additional carbon capture). However, a current bottleneck for green hydrogen production is the availability of sustainable energy sources. In conventional processes, water splitting is achieved by applying an external bias voltage across two electrodes (electrochemical method, Sect. 2.3). This method unfortunately requires large amounts of electricity, which cannot always be met by renewable sources, limiting the overall sustainability of the application. To avoid this issue, an alternative water splitting method has been proposed (see Sect. 2.4), where the energy of sunlight can directly be absorbed by a photocatalyst that drives the reaction to produce hydrogen. In the following sections, an overview of the chemical reactions involved generally in the water splitting process will be given, as well as a more detailed discussion of the different approaches [5, 7].

2.2 Thermodynamic and Kinetic Foundations

The production of hydrogen from water is based on the overall reaction

$$2\,H_2O \longrightarrow 2\,H_2 + O_2. \tag{2.1}$$

If hydrogen is then used as fuel at a later stage, the reaction is reversed, releasing the stored energy and leaving only water behind. The water splitting reaction is highly endothermic, with a Gibbs free energy of $\Delta G° = 237.2\,\mathrm{kJ/mol}$ per H_2O molecule under standard conditions. This corresponds to a thermodynamic potential of 1.23 V and an overall energy difference of approximately 4.92 eV between reactants and products of the complete four-electron reaction in Fig. 2.1. However, this thermodynamic potential represents the minimum equilibrium voltage needed to drive the reaction without considering kinetic losses. The energy required in practice is higher due to inefficiencies in the process, which has motivated extensive efforts to minimize any losses during the reaction [8–10].

2.3 Electrochemical Water Splitting

For the electrochemical process of water splitting, also called electrolysis of water, two electrodes, connected via an external circuit, are typically immersed in electrolyte. An applied bias voltage then induces oxidation and reduction reactions at the cathode and anode. In the electrolyte, charge neutrality is maintained through ion transport between the electrodes. The general reaction can therefore be divided into two redox half-reactions that occur on separate electrodes. On the cathode, the hydrogen evolution reaction (HER) represents the reduction

$$2\,H^+ + 2\,e^- \rightleftharpoons H_2 \tag{2.2}$$

with $E° = 0\,\mathrm{V}$. On the anode, the oxygen evolution reaction (OER) or water oxidation reaction

$$2\,H_2O \rightleftharpoons 4\,H^+ + 4\,e^- + O_2 \tag{2.3}$$

takes place (see Fig. 2.1), where $E° = 1.23\,\mathrm{V}$. $E°$ is the standard electrode potential that refers to the standard hydrogen electrode (SHE) for the relevant redox couple (H^+/H_2 and H_2O/O_2), defining the theoretically required minimum voltage to drive the reaction electrochemically. Among the two half-reactions, the OER is generally considered to be the rate-limiting process due to slower kinetics, arising from its complex four-electron transfer mechanism and the need to form O–O bonds [11, 12]. The whole OER consists of five steps, described in Fig. 2.1, which can be associated with reaction coordinates. These individual reaction states are $2\,H_2O \longrightarrow OH^* + H_2O + H^+ + e^- \longrightarrow O^* + H_2O + 2\,H^+ + 2\,e^- \longrightarrow OOH^* + 3\,H^+ + 3\,e^- \longrightarrow O_2 + 4\,H^+ + 4\,e^-$.

Although the theoretical minimum potential for water splitting is 1.23 V, in practice, higher cell voltages of about 1.6 V to 2.0 V are required due to overpotentials (η) [14, 15]. The total overpotential is typically composed of contributions from activation, concentration and resistance [16]. The activation overpotential (η_{act}) arises from the energy barrier for electron transfer at the electrode surface, which is dominated by the OER.

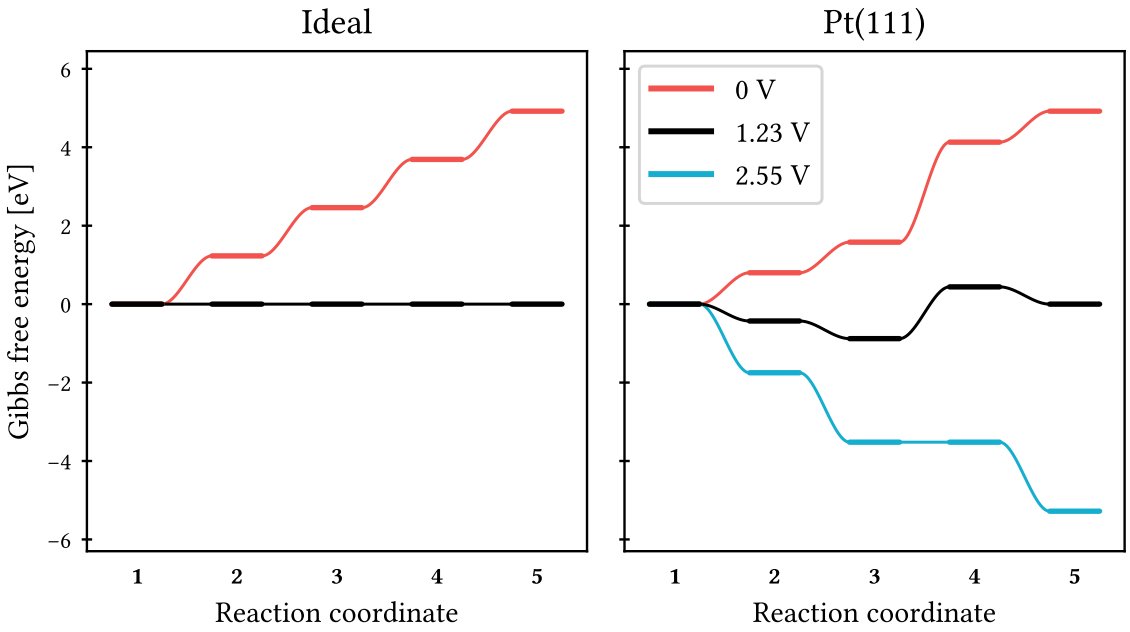

Figure 2.1: Schematic Gibbs free energy diagram of the OER on an ideal surface (left) and a pristine Pt(111) surface (right). The free energy barriers for each intermediate step can be reduced by applying a bias voltage [13]. The reaction coordinates (1–5) denote the following states: $2\,H_2O \longrightarrow OH^* + H_2O + H^+ + e^- \longrightarrow O^* + H_2O + 2\,H^+ + 2\,e^- \longrightarrow OOH^* + 3\,H^+ + 3\,e^- \longrightarrow O_2 + 4\,H^+ + 4\,e^-$.

In addition, the concentration overpotential (η_{conc}) is generated by mass transport limitations such as slow diffusion of reactants or products. Lastly, the resistance or ohmic overpotential (η_{ohm}) appears due to resistance losses in the electrolyte, electrodes, and contacts. These overpotentials lead to the requirement of additional energy and thus reduce the overall efficiency of the water splitting process. For practical applications, the Faradaic efficiency, which quantifies the fraction of transferred electrons that contribute to the desired H_2 and O_2 evolution reactions compared to side reactions, should approach 100 % [17]. Reducing these overpotentials through improved electrocatalyst designs and optimized charge transport is therefore essential for efficient electrochemical water splitting systems. In the HER, this is achieved with Pt-based catalysts, which exhibit a hydrogen adsorption energy near the optimum as well as excellent catalytic activity [15]. However, their high cost and scarcity are disadvantages that have led to the development of alternatives like transition metal sulphides (for example MoS_2) and Ni-based alloys. For the OER, noble metal oxides such as IrO_2 or RuO_2 have excellent catalytic performance, but their limited stability and availability have given rise to earth-abundant alternatives like oxyhydroxides based on Fe and Ni. In addition to the catalytic activity, the long-term material stability is a requirement for practical electrolysis systems. Especially in the OER, the exposure of the electrode to highly oxidative

and corrosive operating conditions can lead to catalyst degradation and reduced efficiency over time. The reliance on noble metal catalysts to reduce this issue increases the cost of large-scale hydrogen production and has motivated ongoing research into stable and earth-abundant alternatives.

2.4 Photoelectrochemical Water Splitting

While electrochemical water splitting offers a technologically mature and efficient approach, its dependence on external electrical energy, especially if produced from non-renewable sources, remains a major limitation (see Sect. 2.3). Therefore, photoelectrochemical (PEC) water splitting, where solar energy in the form of sunlight is directly utilized to drive the water splitting reaction, has gained increased attention. In such systems, semiconductor photoelectrodes absorb visible light to excite electrons to higher energy levels and thus create holes, which in turn participate in the HER and OER at the semiconductor–water interface. This direct pathway for solar-to-hydrogen conversion can, in principle, achieve higher efficiencies than coupled photovoltaic–electrolysis systems by minimizing energy conversion losses, offering a sustainable alternative for green hydrogen production [15].

The principle of PEC water splitting is the integration of light absorption and electrochemistry into a single device. To enable the process, the semiconductor photoelectrode has to satisfy two key thermodynamic requirements. First, the bandgap must be large enough to absorb sunlight effectively. The thermodynamic minimum bandgap of 1.23 eV is determined by the required potential for water splitting, the same as for the electrochemical process. In reality, this minimum is inadequate to drive the reaction due to overpotential losses and kinetic barriers (Sect. 2.3). A bandgap of approximately 1.6 eV to 2.0 eV is therefore usually required. Second, it has to be energetically favourable for the electron to be transferred from the conduction band minimum (CBM) to the proton reduction level (H^+/H_2) and for the hole to be transferred from the valence band maximum (VBM) to the water oxidation level (H_2O/O_2), as illustrated in Fig. 2.2. These band alignments of the semiconductor relative to the redox potentials ensure that it is suitable to drive both the HER and OER upon light absorption. However, in practice, two different materials are often preferred to carry out the reactions separately and thus reduce the requirements and complexity for each of the catalysts [18].

The mechanism of PEC water splitting can be divided into three stages: First, photoexcitation occurs, where sunlight excites electrons to higher energy states and creates holes in the photocatalyst. Then, the charge carriers are transported to the semiconductor–water interface while minimizing recombination losses, where ultimately the surface redox reactions can take place, with the electrons driving the HER and the holes driving the OER. In practice, such systems can be configured either as single photoelectrodes, where the photoanode or photocathode is paired with a counter electrode, or as tandem

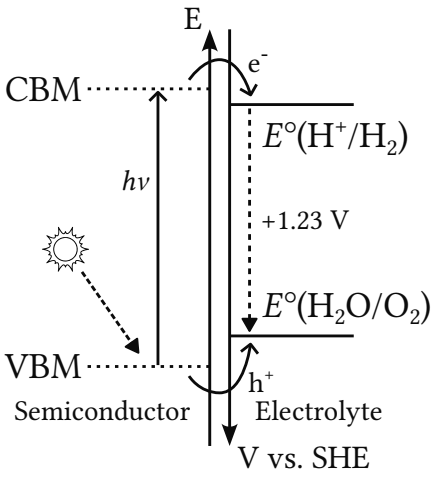

Figure 2.2: Illustration of the band alignment for PEC water splitting.

cells, where photoanode and photocathode are combined to enable unassisted water splitting [18, 19].

For photoanodes, which enable the OER, a popular choice of material is $BiVO_4$, as it allows for visible light absorption and has a favourable VBM. However, some limitations with $BiVO_4$ are poor conductivity and high recombination rates (see Chapter 3) [20, 21]. As an alternative, TiO_2 has been established as a stable and low-cost option, though its wider bandgap limits the absorption to ultraviolet (UV) light. The wide band gap can be reduced through doping, which enables absorption in the visible range, but in turn comes at the expense of a reduced catalytic activity [22, 23]. For photocathodes, which promote the HER, Cu_2O is a common choice. While it can absorb visible light and has a suitable CBM, it can suffer from photocorrosion, which must be prevented through coatings of co-catalysts, like for example Pt or Au [24, 25]. Also Si, which has a high absorption coefficient due to its narrow bandgap, has been suggested as a photocathode, however, it requires surface modifications because of its instability in aqueous electrolytes [26, 27]. Nevertheless, despite the considerable progress achieved with these materials, further optimization of their performance to allow for efficient overall water splitting remains challenging. Although limitations such as charge recombination, instability, and photocorrosion can be mitigated by doping, surface passivation, or the use of co-catalysts, a fundamental trade-off between bandgap and band alignment remains. A narrow bandgap improves the absorption of light, but might not provide sufficient driving force for water splitting. In contrast, a wide bandgap ensures the desired alignment but limits absorption to high-energy photons, excluding most of the visible light spectrum [18, 19].

In its current state, the solar-to-hydrogen efficiency of PEC devices is typically below 5 %, but single trials have managed to achieve around 15 %. However, in order to apply this technology in practice, much higher efficiencies are desired, which could po-

tentially be reached through novel materials with optimal bandgaps, advanced device architecture, and scale-up strategies [28, 29]. Alternatively, devices with lower efficiencies could become of interest, if their cost can be lowered to a level at which their production becomes advantageous. Due to the need for improved photoelectrodes to drive the water splitting process, improved materials that show increased efficiency (or lower cost) are of great significance. Such improvements are typically connected closely to a material's intrinsic properties like the electronic structure. Therefore, understanding the fundamentals of charge transport and localization within a photocatalyst is of high importance. This thesis focuses on the photoanode material $BiVO_4$ (Chapter 3) to investigate different charge trapping mechanisms and mobility of localized charges (Chapter 5) using computational approaches (Chapter 4).

3

The Material: Bismuth Vanadate

Bismuth vanadate ($BiVO_4$) is a visible-light-active semiconductor that has attracted increasing attention as a promising photoelectrode for the water splitting reaction (see Chapter 2) [20, 30]. Its layered crystal structure is constructed of VO_4 tetrahedra that are interconnected via BiO_8 polyhedra. While $BiVO_4$ can be synthesized in several polymorphic forms, the room temperature monoclinic scheelite (ms) phase of space group $I2/b$ is the most experimentally relevant [31]. $BiVO_4$ exhibits a strong tendency for charge localization, caused by a pronounced electron–phonon coupling that aids the stabilization of small polarons and STEs (see Chapter 5). For these reasons, it represents an attractive model system to explore the interplay between lattice distortions and excited-state dynamics in transition metal oxides [32, 33]. In this thesis, $BiVO_4$ is used as a platform to study the formation, stability, and kinetic behaviour of STEs applying first-principles methods.

3.1 Crystal Structure and Charge Localization

The crystal structure of $BiVO_4$ plays an important role in the electronic and optical properties of the material. It is worth noting that there are two closely related scheelite phases. Ms-$BiVO_4$ is the low-temperature ground state that transforms into the tetragonal scheelite (ts) phase of space group $I4_1/a$ at a temperature of around 528 K [31, 34]. However, structural relaxation of ms-$BiVO_4$ using semi-local exchange–correlation functionals typically leads to the formation of ts-$BiVO_4$ already at 0 K due to the inadequate description of the Bi lone-pair electrons. Although hybrid functionals can recover the ms structure, the required high fraction of exact exchange [35] and the physical origin of this sensitivity [35, 36] are still discussed. In ms-$BiVO_4$, a distorted variant of the higher-symmetry ts-$BiVO_4$, two inequivalent V–O bond lengths are present [37]. This

distortion arises from the asymmetric coordination of the Bi atoms that form BiO_8 polyhedra, while the V centres arrange as VO_4 tetrahedra [31]. The deviation is, however, very subtle and not distinguishable in Fig. 3.1, hence only the ts structure is shown. Due to this small structural difference, the ts-$BiVO_4$ structure is often, including this thesis, used as a simplified model. For charge localization and transport, this can be motivated by previous work finding very similar electronic band structures, electron-polaron states, and almost identical hopping barriers in the two phases [38, 39]. Nevertheless, some experimental studies report different photocatalytic or photoelectrochemical performance for ts and ms samples [20, 37, 40]. However, the samples were produced using different synthesis or treatment conditions, so morphology, crystallinity, defects, and surfaces may also explain the difference. It is therefore not fully established whether the small structural differences between the bulk phases significantly affect charge transport and photocatalytic performance [36].

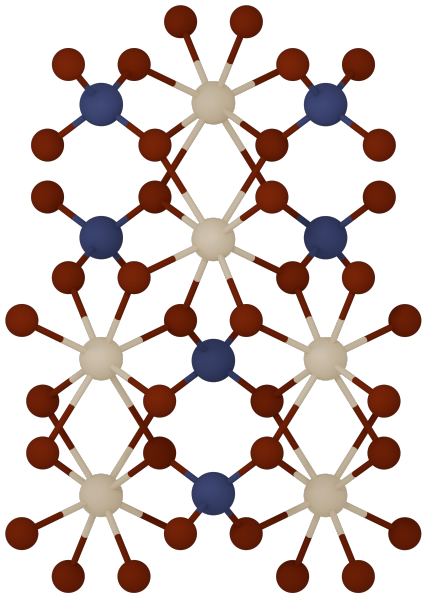

Figure 3.1: The crystal structure of ts-$BiVO_4$. Bi atoms are shown in beige, V in dark blue and O in dark red.

$BiVO_4$ is a promising material for PEC water splitting, as its indirect bandgap of about 2.4 eV to 2.5 eV lies in the visible spectrum and therefore allows the absorption of visible light [41, 42]. Furthermore, its valence and conduction band edges are thermodynamically aligned to drive the OER, making it a model photoanode material. However, the most important property is the strong tendency for charge localization, which leads to electrons and holes in $BiVO_4$ not remaining delocalized upon photoexcitation but rather creating small polarons. The electrons thereby localize on V sites, while the holes form primarily on O sites with hybridized Bi–O character. This phenomenon occurs because

of the strong electron–phonon coupling that prevails in the material, which lowers the energy of the system by distorting the lattice around the charge carrier [20]. In addition, the anisotropic nature of $BiVO_4$ modulates the mobility of these polarons and influences the formation of STEs, as elaborated in more detail in Chapter 5 [32].

3.2 Evidence for Charge Trapping

Due to $BiVO_4$'s particular combination of electronic, optical, and structural properties, it is not only a promising photocatalyst for the water splitting reaction, but also portrays an exceptional material for investigating the fundamentals of STEs and their less known dynamic behaviour in the context of this thesis. Firstly, the strong electron–phonon coupling stabilizes localized charge carriers and thereby aids the formation of small polarons and STEs, like presented in Fig. 3.2. Secondly, visible light absorption, enabled by a suitable bandgap, facilitates experimental accessibility in the form of direct observations of excited-state dynamics through the use of techniques like photoluminescence and transient absorption spectroscopy. And thirdly, the well-characterized crystal structure offers the possibility for accurate first-principles modelling, where hybrid functionals (see Chapter 4) are applied to capture the charge localization and excited-state behaviour.

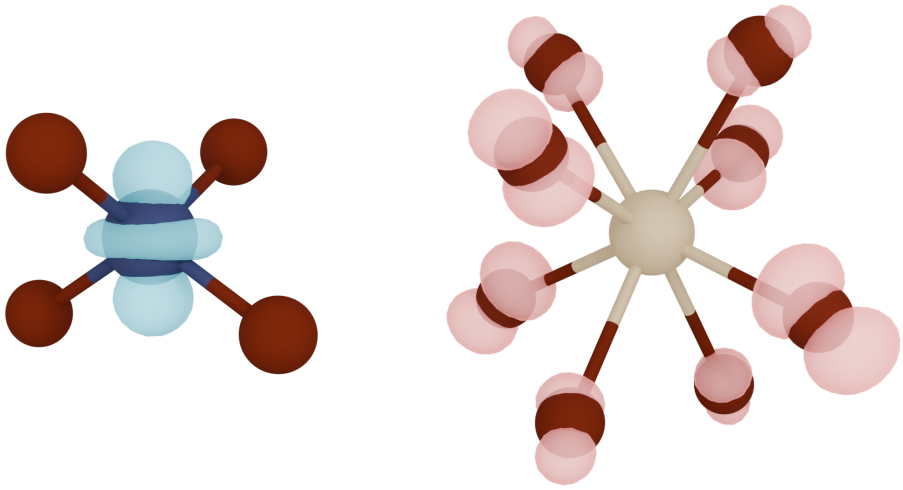

(a) (b)

Figure 3.2: Polarons in $BiVO_4$, calculated using electronic structure theory. Illustrations show the charge isosurfaces of an excess a) electron and b) hole.

Previously, the existence of STEs in $BiVO_4$ has been observed experimentally in the form of polaron emission peaks that can be assigned to the trapping of electrons and holes [43, 44]. These findings are confirmed by our studies, which have shown that

$BiVO_4$ hosts two distinct configurations of STEs, both exhibiting unique spatial and energetic characteristics, which are in more detail discussed in Chapter 6. In the first type, STE1, the electron localizes on a V site, with the hole forming on the O atoms of a neighbouring BiO_8 polyhedron, creating a more extensive electron–hole pair. Conversely, while in the second type, STE2, the electron is localized on a V site as well, the hole arises on an O atom of the same VO_4 tetrahedra, leading to a rather compact shape. One of the key findings from studying STEs in $BiVO_4$ is that both STE types possess a comparable formation energy, which suggests that both are of experimental relevance and may coexist under typical conditions. This aligns well with the general theory of STEs discussed in Chapter 5, which presents an explanation for how bound electron–hole pairs can localize and distort the lattice of a material. An additional discovery in $BiVO_4$ is that a single STE configuration can produce multiple emission peaks in the photoluminescence spectrum that originate from transitions between localized and delocalized states within the exciton. This is consistent with experimental photoluminescence studies, where broad and asymmetric emission bands were observed in $BiVO_4$ thin films [45]. Beyond static properties, also the kinetic behaviour of STEs in $BiVO_4$ can be analyzed. These investigations reveal that both STE types show distinct kinetic pathways, with energy barriers for hopping, dissociation and transformation processes ranging from tens to several hundreds of meV, corresponding to time delays between femto- and nanoseconds. Comparing this barrier-based mechanistic picture with results from transient absorption measurements reveals a good agreement for STE dynamics in $BiVO_4$ [43, 44].

Slower trapping pathways (on microsecond time scales) in $BiVO_4$ can be enabled by alternative charge trapping mechanisms like, for example, O–O hole dimers. Their formation and trapping of an extra electron provide an additional route for charge localization. The coexistence of STEs and hole dimers offers an explanation for the wide range of time scales observed in experimental studies of charge trapping and recombination.

Overall, using $BiVO_4$ as a model system, the first-principles calculations not only elucidate the nature of STEs in $BiVO_4$ but also provide a quantitative framework for understanding their stability, mobility and emission properties. The insights gained through this material contribute also to the broader discussion of excited-state dynamics in transition metal oxides in general, as discussed in more detail in Chapter 5, and demonstrate the power of advanced computational methods like described in Chapter 4.

3.3 Synthesis and Structural Control

The synthesis conditions of $BiVO_4$ can have a significant influence on its structural and electronic properties, including charge-carrier transport and excited-state dynamics. The most commonly employed synthesis procedures are hydrothermal and sol–gel

methods, which under conditions above room temperature yield $BiVO_4$ in the photoactive ms phase. However, phase formation during synthesis depends on parameters such as temperature, precursor chemistry, and pH [20, 30]. Although metastable ts-$BiVO_4$ can be obtained under carefully controlled synthesis conditions at lower temperatures, thermal treatment is typically required to promote transformation from the ms phase to the ts phase. While the phase transformations are normally reversible, either through grinding or heating of the material, ms is generally seen as the low-temperature structure, while ts is prominent at high temperatures [30, 46, 47]. Regarding the computational simulations described in this thesis (Chapter 4), ts was the phase of choice, since in the simulation environment it is already stable at 0 K, and electronic properties show small differences [38, 39].

In addition to phase selection, the properties of the material can also be modulated through structural tuning. For example, epitaxial strain in thin films has been demonstrated to alter the electronic structure, bandgap, and charge localization characteristics of $BiVO_4$ [45, 48]. Such strain effects may influence the formation and stability of polarons and STEs, making them relevant for both experimental and computational studies.

4

The Methods: Electronic Structure Theory

4.1 Quantum Mechanical Many-Electron Problem

The many-electron problem is a fundamental cornerstone of quantum mechanics, where the goal is to solve the Schrödinger equation for systems containing multiple electrons and nuclei. Understanding the electronic structure of such systems is essential for predicting chemical reactivity, material properties, and molecular behaviour. The time-independent Schrödinger equation,

$$\hat{H}\Psi = E\Psi, \tag{4.1}$$

describes the energy E of a stationary state with wave function Ψ containing all electronic and nuclear degrees of freedom as coordinates as well as the Hamiltonian $\hat{H}$. In atomic units, Planck's reduced constant $\hbar$, the electron mass m, the elementary charge e, and the term $\frac{1}{4\pi\varepsilon_0}$ are set to 1. The non-relativistic Hamiltonian can then be written as

$$\begin{aligned}\hat{H} = &\underbrace{-\frac{1}{2}\sum_{i=1}^{N}\Delta_i}_{\hat{T}} \underbrace{+\frac{1}{2}\sum_{i,j\neq i}\frac{1}{|\boldsymbol{r}_i-\boldsymbol{r}_j|}}_{\hat{V}_{\mathrm{ee}}} \\ &\underbrace{-\sum_{i=1}^{N}\sum_{k=1}^{K}\frac{Z_k}{|\boldsymbol{r}_i-\boldsymbol{R}_k|}}_{\hat{V}_{\mathrm{en}}} \underbrace{-\sum_{k=1}^{K}\frac{1}{2M_k}\Delta_k}_{\hat{T}_{\mathrm{n}}} \underbrace{+\frac{1}{2}\sum_{k,l\neq k}\frac{Z_k Z_l}{|\boldsymbol{R}_k-\boldsymbol{R}_l|}}_{\hat{V}_{\mathrm{nn}}}\end{aligned} \tag{4.2}$$

for a system of N electrons with coordinates $\boldsymbol{r}_i$, K atomic nuclei with coordinates $\boldsymbol{R}_k$, the corresponding charge numbers Z_k and masses M_k. Here, $\hat{T}$ and $\hat{T}_\mathrm{n}$ represent the kinetic energy of the electrons and nuclei, respectively. $\hat{V}_\mathrm{ee}$ and $\hat{V}_\mathrm{nn}$ describe the electron–electron and nuclei–nuclei Coulomb repulsion, while $\hat{V}_\mathrm{en}$ is the electron–nuclei attraction. The factor of $\frac{1}{2}$ in $\hat{V}_\mathrm{ee}$ and $\hat{V}_\mathrm{nn}$ avoids double-counting of pairwise interactions. However, this equation can only be solved analytically for one-electron systems due to the exponential complexity introduced by the coupled degrees of freedom of multiple particles [49].

To simplify the problem above, the so-called Born–Oppenheimer approximation has been introduced, which exploits the large mass difference between electrons and nuclei. Since nuclei are significantly heavier than electrons, their motion is much slower, allowing the electronic and nuclear degrees of freedom to be decoupled [50]. Under this approximation, the nuclei are treated as fixed, and the Hamiltonian can be defined for electrons that experience the Coulomb potential of stationary nuclei, whose kinetic energy is neglected:

$$\hat{H} = \underbrace{-\frac{1}{2}\sum_{i=1}^{N}\Delta_i}_{\hat{T}} \underbrace{+\frac{1}{2}\sum_{i,j\neq i}\frac{1}{|\boldsymbol{r}_i-\boldsymbol{r}_j|}}_{\hat{V}_\mathrm{ee}} \underbrace{+\sum_{i=1}^{N}v(\boldsymbol{r}_i)}_{\hat{V}_\mathrm{ext}}, \tag{4.3}$$

where $\hat{V}_\mathrm{ext}$ is the external potential, which is the sum of contributions of the local potential $v(\boldsymbol{r})$ of the electrostatic field of all the fixed nuclei acting on an electron

$$v(\boldsymbol{r}) = -\sum_{k=1}^{K}\frac{Z_k}{|\boldsymbol{r}-\boldsymbol{R}_k|}. \tag{4.4}$$

However, even with this simplification, solving the Schrödinger equation for systems with more than one electron remains impossible. This has motivated the development of approximation methods, which provide practical frameworks for describing the electronic structure. Popular approaches are on the one hand the Hartree–Fock approximation and its extensions, where the wave function is approximated, and on the other hand density functional theory (DFT), where the total energy is obtained through the density [51].

4.2 Hartree–Fock Method

The Hartree–Fock method makes use of the Rayleigh–Ritz variational principle, which states that for any state $|\Psi\rangle$, the expectation value of the Hamiltonian,

$$E[\Psi] = \frac{\langle\Psi|\hat{H}|\Psi\rangle}{\langle\Psi|\Psi\rangle} \geq E_0, \tag{4.5}$$

is always greater than or equal to the true ground state energy E_0. Thus, the best approximation for the ground state is characterized by the minimum of $E[\Psi]$, yielding the closest possible value to the ground state energy.

In the Hartree–Fock approximation, the many-electron wavefunction Ψ is written as a Slater determinant of single-particle orbitals $\varphi_i(\boldsymbol{r})$:

$$\Psi(r_1, r_2, \dots, r_n) = \frac{1}{\sqrt{N!}} \begin{vmatrix} \varphi_1(r_1) & \varphi_2(r_1) & \dots & \varphi_N(r_1) \\ \varphi_1(r_2) & \varphi_2(r_2) & \dots & \varphi_N(r_2) \\ \vdots & \vdots & & \vdots \\ \varphi_1(r_N) & \varphi_2(r_N) & \dots & \varphi_N(r_N) \end{vmatrix}. \tag{4.6}$$

This form ensures that the wavefunction is anti-symmetric with respect to the interchange of two particles, thereby satisfying the Pauli exclusion principle, which states that no two electrons can occupy the same state. The Hartree–Fock equations are derived by making use of the variational principle (minimizing $E[\Psi]$) under the constraint that the single-particle orbitals remain orthonormal,

$$\left[\hat{h}(\boldsymbol{r}) + v_{\mathrm{H}}(\boldsymbol{r})\right] \varphi_i(\boldsymbol{r}) - \int v_{\mathrm{x}}(\boldsymbol{r}, \boldsymbol{r}')\varphi_i(\boldsymbol{r}')\mathrm{d}\boldsymbol{r}' = \varepsilon_i \varphi_i(\boldsymbol{r}). \tag{4.7}$$

Here, $\hat{h}(\boldsymbol{r})$ is the one-particle operator (kinetic energy and external potential) and $v_{\mathrm{H}}(\boldsymbol{r})$ is the Hartree potential (classic Coulomb repulsion). A third non-local term called the Fock exchange potential is added, which accounts for quantum exchange effects and lowers the energy compared to the pure Hartree solution. However, the accuracy of the Hartree–Fock solution is limited in many applications, since correlation effects are not described beyond the classical mean-field Coulomb interaction represented by v_{H}. To address this, alternative approaches such as DFT have been developed and are preferred in practice, as they include correlation effects at a comparable or lower computational cost [51].

4.3 Hohenberg–Kohn Theorem

A fundamental understanding of DFT is achieved by the Hohenberg–Kohn theorem. It shows that the ground state potential of a system in an external potential $v_{\mathrm{ext}}(\boldsymbol{r})$ is uniquely defined up to a constant by its density $n(\boldsymbol{r})$. The total energy $E[n(\boldsymbol{r})]$ of the system can therefore be expressed as a functional of the electronic density as

$$E[n(\boldsymbol{r})] = \int v_{\mathrm{ext}}(\boldsymbol{r}) n(\boldsymbol{r}) \mathrm{d}\boldsymbol{r} + F[n(\boldsymbol{r})], \tag{4.8}$$

where the first term represents the contribution of the external potential and results in the external energy $E_{\mathrm{ext}}[n(\boldsymbol{r})]$. The second term $F[n(\boldsymbol{r})]$ describes the electron–electron

interactions, which can in turn be split up into the Coulomb interaction (or Hartree term $E_{\mathrm{H}}[n(\boldsymbol{r})]$) and a universal functional $G[n(\boldsymbol{r})]$ that accounts for all quantum mechanical effects beyond the classical Coulomb interaction:

$$F[n(\boldsymbol{r})] = \frac{1}{2}\iint \frac{n(\boldsymbol{r})n(\boldsymbol{r}')}{|\boldsymbol{r}-\boldsymbol{r}'|}\mathrm{d}\boldsymbol{r}\mathrm{d}\boldsymbol{r}' + G[n(\boldsymbol{r})]. \tag{4.9}$$

With this, the many-body electron problem can successfully be reformulated in terms of the electronic density, which now serves as the fundamental variable of the system. However, the exact form of $G[n(\boldsymbol{r})]$, which contains the kinetic energy and quantum mechanical effects, is unknown and must be determined in practice through further approximations [52].

4.4 Kohn–Sham Equations

To approximate the universal functional $G[n(\boldsymbol{r})]$, Kohn and Sham [53] proposed replacing the system of interacting electrons with a non-interacting system with the same properties. This allows for a description using only single-particle equations in an effective potential. The universal functional can then be written as

$$G[n(\boldsymbol{r})] = T_{\mathrm{S}}[n(\boldsymbol{r})] + E_{\mathrm{xc}}[n(\boldsymbol{r})] \tag{4.10}$$

with the kinetic energy of a system of non-interacting electrons $T_{\mathrm{S}}[n(\boldsymbol{r})]$, which can be calculated exactly, and the exchange and correlation energy of the interacting system $E_{\mathrm{xc}}[n(\boldsymbol{r})]$ [53]. This allows rewriting the total energy functional as

$$E[n(\boldsymbol{r})] = E_{\mathrm{ext}}[n(\boldsymbol{r})] + E_{\mathrm{H}}[n(\boldsymbol{r})] + T_{\mathrm{S}}[n(\boldsymbol{r})] + E_{\mathrm{xc}}[n(\boldsymbol{r})]. \tag{4.11}$$

The ground state energy density can be obtained from the eigenstates (called the single-particle or Kohn–Sham orbitals $\varphi_i(\boldsymbol{r})$) of the Kohn–Sham equations,

$$\left[-\frac{1}{2}\Delta + v_{\mathrm{S}}(\boldsymbol{r})\right]\varphi_i(\boldsymbol{r}) = \varepsilon_i\varphi_i(\boldsymbol{r}), \tag{4.12}$$

with the Kohn–Sham eigenvalues ε_i and the Kohn–Sham potential

$$v_{\mathrm{S}}(\boldsymbol{r}) = v_{\mathrm{ext}}(\boldsymbol{r}) + v_{\mathrm{H}}(\boldsymbol{r}) + v_{\mathrm{xc}}(\boldsymbol{r}) \tag{4.13}$$

containing the external potential $v_{\mathrm{ext}}(\boldsymbol{r})$, the Hartree potential $v_{\mathrm{H}}(\boldsymbol{r})$ and the exchange–correlation potential $v_{\mathrm{xc}}(\boldsymbol{r})$ [51]. The exchange–correlation potential is in turn defined as the derivative of the exchange–correlation energy with respect to the density,

$$v_{\mathrm{xc}}(\boldsymbol{r}) = \frac{\delta E_{\mathrm{xc}}[n(\boldsymbol{r})]}{\delta n(\boldsymbol{r})}. \tag{4.14}$$

Combining the equations above, the total energy of the system can be expressed as

$$E = \sum_{i=1}^{N} \varepsilon_i - E_{\mathrm{H}} + E_{\mathrm{xc}} - \int v_{\mathrm{xc}}(\boldsymbol{r}) n(\boldsymbol{r}) \mathrm{d}\boldsymbol{r}. \tag{4.15}$$

The Kohn–Sham equations are solved self-consistently by starting from an initial guess and iteratively calculating the single-electron equations and updating the density and potential until convergence is achieved [53]. The implementation of this process is discussed in more detail in Sect. 4.7.4.

4.5 Exchange–Correlation Functionals

While the expressions for the exchange–correlation energy provide a theoretical foundation for DFT calculations, the exact form of $E_{\mathrm{xc}}[n(\boldsymbol{r})]$ is not known. Thus, approximations need to be introduced. In the following, an overview of the most common approaches to computing the exchange–correlation energy is provided.

4.5.1 Local Density Approximation

The simplest and still widely used approximation is the local density approximation (LDA). In the LDA, the assumption is made that the total exchange–correlation energy of a density distribution $n(\boldsymbol{r})$ can be approximated as the sum of local contributions from a uniform electron gas with the same density. This leads to expressing $E_{\mathrm{xc}}[n(\boldsymbol{r})]$ as

$$E_{\mathrm{xc}}^{\mathrm{LDA}}[n(\boldsymbol{r})] = \int n(\boldsymbol{r}) e_{\mathrm{xc}}^{\mathrm{unif}}[n(\boldsymbol{r})] \mathrm{d}\boldsymbol{r} \tag{4.16}$$

depending only on the density at a point and the exchange–correlation energy per particle of a uniform electron gas $e_{\mathrm{xc}}^{\mathrm{unif}}[n(\boldsymbol{r})]$. Since the exchange and correlation energies for a uniform electron gas are known, this approximation can be computed efficiently [54]. The LDA is by construction exact for a uniform density and nearly-exact for slowly varying densities, making it well suited for describing simple metals. However, among other limitations, it obviously does not incorporate inhomogeneity or gradient corrections and is not exact in the one-electron limit [55]. This leads in many cases to an underestimation of the lattice parameter of solids and the bond lengths in molecules.

4.5.2 Generalized Gradient Approximation

One more advanced way of approximating the exchange–correlation functional is the generalized gradient approximation (GGA), where both the density and its gradient are taken into account. This allows for eliminating some of the disadvantages of LDA, while

keeping its good properties. A widely used functional has been developed by Perdew, Burke, and Ernzerhof (PBE) [56], where the simpler LDA functional is modulated by the enhancement factor $F_{\mathrm{xc}}[n(\boldsymbol{r}), \nabla n(\boldsymbol{r})]$. In the limit of the uniform electron gas, this approximation will therefore yield the same results as LDA. The PBE–GGA functional has the form of

$$E_{\mathrm{xc}}^{\mathrm{GGA}}[n(\boldsymbol{r})] = \int n(\boldsymbol{r}) e_{\mathrm{xc}}^{\mathrm{unif}}[n(\boldsymbol{r})] F_{\mathrm{xc}}[n(\boldsymbol{r}), \nabla n(\boldsymbol{r})] \mathrm{d}\boldsymbol{r} \tag{4.17}$$

with $e_{\mathrm{xc}}^{\mathrm{unif}}[n(\boldsymbol{r})]$ again representing the exchange–correlation energy per particle of a uniform electron gas. The PBE–GGA functional presents an overall improvement compared to LDA, however, it overshoots and produces too large lattice parameters or bond lengths in many cases [51].

4.5.3 Hybrid Density Functionals

A common approach to further improve accuracy is the application of hybrid functionals. The key idea is to incorporate a fraction of the exact Hartree–Fock exchange (see Sect. 4.2) into the exchange–correlation functional, rather than relying solely on semi-local approximations like PBE. This generally improves the description of atomization energies, bond lengths, and vibrational frequencies of most molecules [51]. The explanation for this can be found by taking a closer look at the coupling constant expression for E_{xc},

$$E_{\mathrm{xc}} = \int_0^1 \mathrm{d}\lambda \, \langle \Psi_n^{\mathrm{min},\,\lambda} | \hat{V}_{\mathrm{ee}} | \Psi_n^{\mathrm{min},\,\lambda} \rangle - U. \tag{4.18}$$

Approximating this integral using the trapezoidal rule yields

$$E_{\mathrm{xc}} \approx \frac{1}{2}(E_{\mathrm{xc},\,\lambda=0} + E_{\mathrm{xc},\,\lambda=1}) = \frac{1}{2}(E_{\mathrm{x}} + E_{\mathrm{xc},\,\lambda=1}), \tag{4.19}$$

where in the non-interacting case ($\lambda = 0$), the correlation energy vanishes, and only the exact exchange energy remains. It has been argued that local or semi-local density functionals are more accurate in the fully-interacting case ($\lambda = 1$), since the exchange–correlation hole is deeper and more localized around each electron compared to the non-interacting case ($\lambda = 0$). The remaining term, the unknown $E_{\mathrm{xc},\,\lambda=1}$, can be approximated using some semi-local (sl) functional, for example LDA or GGA [57]. This leads to the introduction of Becke's half–half hybrid functional [58],

$$E_{\mathrm{xc}} = \frac{1}{2}(E_{\mathrm{x}} + E_{\mathrm{xc},\,\lambda=1}^{\mathrm{sl}}) = E_{\mathrm{xc}}^{\mathrm{sl}} + \frac{1}{2}(E_{\mathrm{x}} - E_{\mathrm{x}}^{\mathrm{sl}}). \tag{4.20}$$

However, it has been found that in many cases, the linear λ-dependence assumed above is not optimal, but a more rapid decay is realistic [57]. Thus, the expression for the

hybrid functional can be written in a more general form,

$$E_{\mathrm{xc}}^{\mathrm{hyb}} = E_{\mathrm{xc}}^{\mathrm{sl}} + \frac{1}{m}(E_{\mathrm{x}} - E_{\mathrm{x}}^{\mathrm{sl}}). \tag{4.21}$$

For $m = 2$, this reproduces the half–half hybrid functional, while for $m = 4$, the so-called PBE0 hybrid functional is obtained, defined as

$$E_{\mathrm{xc}}^{\mathrm{PBE0}} = E_{\mathrm{xc}}^{\mathrm{PBE}} + \frac{1}{4}(E_{\mathrm{x}} - E_{\mathrm{x}}^{\mathrm{PBE}}) = \frac{3}{4}E_{\mathrm{x}}^{\mathrm{PBE}} + \frac{1}{4}E_{\mathrm{x}} + E_{\mathrm{c}}^{\mathrm{PBE}}. \tag{4.22}$$

With PBE0, a significant improvement compared to GGA can be observed when describing molecular properties as well as in solid-state applications. This is due to the fact that the self-interaction error of the density functional (inherent in the Hartree energy) is reduced by including a fixed portion of the Fock exchange [59].

4.6 Transition States

In DFT calculations, the energy of a system is minimized by optimizing its geometric structure until the lowest possible energy is reached, corresponding to a local minimum on the energy surface. To go from one stable state to another (from one local minimum to another one), the system must overcome a specific energy barrier. This barrier depicts the so-called transition state, a higher-energy configuration between the two stable states. It can therefore be understood as a saddle point on the potential energy surface. Since the transition state (and its associated energy barrier) determines the reaction rate, it is essential to identify not just any saddle point, but the lowest-energy saddle point connecting the two investigated minima [60].

The nudged elastic band (NEB) method is a widely used algorithm for locating such transition states [60]. For that, an initial pathway composed of a series of interconnected images (evolving structures along the reaction coordinate) is constructed and subsequently optimized. All intermediate configurations are optimized simultaneously while maintaining the pathway through spring forces until convergence is reached, and the arrangement with the highest energy is identified. This highest-energy image is treated differently from the other images in the climbing image (CI) NEB method: instead of minimizing its energy, the component of the force along the tangent is inverted, effectively "climbing" to the saddle point [60]. Meanwhile, the forces perpendicular to the path continue to minimize the energy, ensuring convergence to the true transition state. The total force $\boldsymbol{F}$ acting on an image of the path in the NEB approach is given by

$$\boldsymbol{F} = \boldsymbol{F}_{\mathrm{S}\parallel} - \nabla E(\boldsymbol{R})_{\perp}, \tag{4.23}$$

where $\boldsymbol{F}_{\mathrm{S}\parallel}$ is the spring force that acts along the local tangent and $\nabla E(\boldsymbol{R})_{\perp}$ is the true force perpendicular to the local tangent.

4.7 Implementation

The popularity of DFT methods in theoretical solid-state physics and quantum chemistry is continuously growing, not least promoted by the number of available software packages for a wide range of applications. While the underlying theory behind these codes is the same, relying on the concepts discussed above, the details of the algorithms and simulation environments can vary significantly. Due to this, the main considerations of different implementations are summarized here.

4.7.1 Boundary Conditions and Supercells

A key challenge in solid-state studies of defect-induced phenomena is balancing the size of the system under investigation. On one hand, realistic descriptions of physical behaviour often require large (ideally infinite) systems to account for extensive crystal rearrangements, on the other hand, computational feasibility demands that the system's size remains as small as possible. This challenge can be navigated by applying the concept of periodic boundary conditions. This allows the study of structured materials (like crystals) as extended systems without needing to consider all of the millions of atoms present in even the smallest crystalline sample. The idea is to include only one unit cell of the material explicitly in the calculations, while the surrounding recurring continuation of the model is implicitly included through periodicity (see Fig. 4.1). However, in many cases, a single unit cell is too small to realistically showcase the

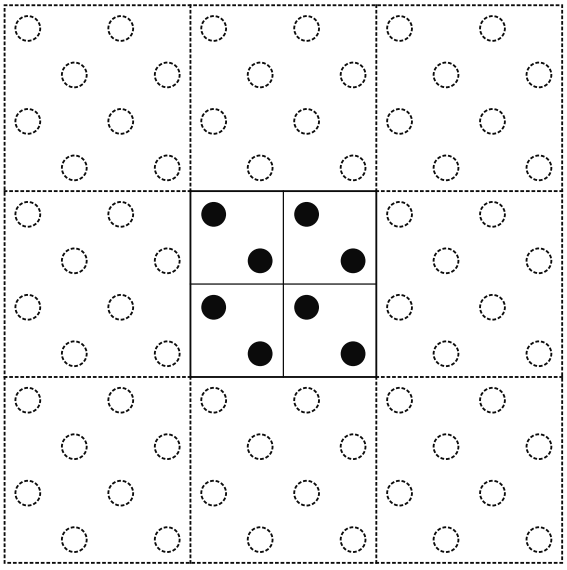

Figure 4.1: Sketch of a supercell (8 atoms) that contains several unit cells (2 atoms). Periodic boundary conditions implicitly extend the system in every direction.

emergence of studied phenomena, as they can arise over areas much larger than the lattice constant. This motivates the introduction of so-called supercells. A supercell consists of several unit cells that are explicitly included in the simulation, creating a sufficiently large system to describe the phenomena of interest with satisfactory precision (Fig. 4.1). This is particularly important for studying extended features, such as defects, surfaces, or localized excitations. The exact size of a supercell can vary greatly depending on the type and order of the system, ranging from a few unit cells to several hundred atoms, and must be determined through convergence testing. By creating large enough supercells, even partially disordered systems, such as liquids, gases, and their interfaces with solids, can be studied.

4.7.2 Basis Sets

One of the characteristic features of a DFT code is the type of basis function that is used to solve the Kohn–Sham equations (see Sect. 4.4). The choice of basis set is critical, as it determines the efficiency and accuracy of the calculation, as well as the types of systems that can be studied. The solution of the Kohn–Sham equations is generally achieved by expanding the Kohn–Sham orbitals $\varphi_i(\boldsymbol{r})$ in terms of known basis functions $\phi_j(\boldsymbol{r})$:

$$\varphi_i(\boldsymbol{r}) = \sum_j c_j^{(i)} \phi_j(\boldsymbol{r}). \tag{4.24}$$

In the following, a brief overview of the main ideas of basis sets, which fulfil periodic boundary conditions that are suitable for crystalline solids, is provided. Such basis sets are, among others, the plane-wave or the slightly more advanced augmented plane-wave basis set.

4.7.2.1 Plane Waves

To simulate the system, the periodicity of its Bravais lattice is reproduced using an external potential in which the electrons move. Plane waves are a natural choice for periodic systems because they inherently satisfy the periodic boundary conditions of the crystal lattice. Applying the Bloch theorem [61], the Kohn–Sham orbitals can be expanded as

$$\varphi_k(\boldsymbol{r}) = \frac{1}{\sqrt{\Omega}} \sum_{\boldsymbol{G}} c_{\boldsymbol{G}}(\boldsymbol{k}) e^{i(\boldsymbol{k}+\boldsymbol{G})\boldsymbol{r}}. \tag{4.25}$$

Here, $\boldsymbol{G}$ denotes the reciprocal lattice vector. The expansion coefficients $c_{\boldsymbol{G}}(\boldsymbol{k})$ are the Fourier coefficients of a particular Bloch wave for a given wave vector $\boldsymbol{k}$. The potential is truncated to include only contributions sufficient to describe electrons in the first Brillouin zone, while maintaining lattice periodicity. This assumption is made to reduce the computational work as much as possible [51].

4.7.2.2 Gaussians

Another widely used method employs Gaussian functions to approximate the molecular orbitals of electrons. In this basis, the Kohn–Sham wavefunctions can be expressed in polar coordinates as

$$\varphi_i(r,\theta,\gamma) = \sum_{nlm} c_{nlm}^{(i)} N Y_{lm}(\theta,\gamma) r^{2n-2-l} e^{-\zeta r^2}, \tag{4.26}$$

where N is a normalization constant, $Y_{lm}(\theta,\gamma)$ are spherical harmonic functions, and n, l and ζ are shape-determining parameters. Gaussian basis sets are popular because they allow for an analytical evaluation of some electron repulsion integrals and thus efficient computations. Additionally, the product of two Gaussians centred at different points yields another Gaussian, further simplifying integral calculations. Gaussian functions can also be combined to mimic the behaviour of Slater-type orbitals, which are more physically accurate but computationally expensive. Due to these reasons, Gaussian basis sets are particularly well-suited for molecular systems, as they can efficiently describe localized molecular orbitals while maintaining computational tractability [62].

4.7.2.3 Projector Augmented Waves

One approach to describe an atomic system is the projector augmented waves (PAW) method, which partitions the atomic-centred wavefunction into two regions. In the valence region, a smooth wavefunction is implemented, acting as an envelope function. In the near-core region, a rapidly oscillating wavefunction is defined, which is then replaced with a smooth pseudo-wavefunction through a transition operator. This division allows for an efficient and accurate description of both the smooth valence states and the rapidly varying core states, combining the benefits of plane waves (for the valence region) with the accuracy of all-electron methods (for the core region)[63].

4.7.3 Pseudopotentials

The concept of pseudopotentials has been introduced firstly to reduce the number of electrons that are to be treated, which is already useful for basis sets other than plane waves, and secondly to make wavefunctions smoother, so fewer plane waves are needed. The goal here is to construct an effective potential that can replace the all-electron potential in a way that core states are eliminated and the valence electrons are described by pseudo-wavefunctions with significantly fewer nodes close to the atomic nuclei, as shown in Fig. 4.2. This allows the pseudo-wavefunctions to be represented using far fewer plane waves, significantly reducing the computational cost. Pseudopotentials are particularly important in plane-wave DFT, as they enable a dramatic reduction in the number of plane waves required to describe the system and make these calculations possible with sufficient accuracy for the chemically relevant valence states. In

this approach, only the chemically active valence electrons are treated explicitly, while the core electrons remain fixed and are seen together with the nuclei as rigid, non-polarizable ion cores.

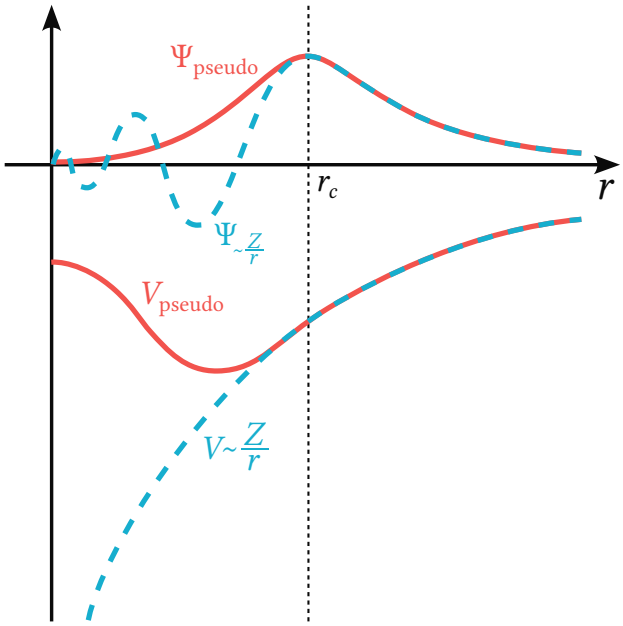

Figure 4.2: Comparison of a wavefunction in the Coulomb potential of the nucleus (blue) to the one in the pseudopotential (red). The real and the pseudo-wavefunctions and potentials match above a certain cutoff radius r_c.

4.7.4 Self-Consistency Algorithm

The computational steps required for DFT calculations are implemented in a self-consistent manner. The self-consistent approach is necessary because the effective potential depends on the electron density, which in turn depends on the effective potential. This circular dependency requires an iterative process to reach a consistent solution. As illustrated in Fig. 4.3, the process begins by taking an initial guess of the electron density, which is used to calculate the effective potential. The Kohn–Sham equations can then be solved and a new value for the electron density and energy is obtained. This procedure is repeated iteratively until the convergence criteria are reached. Once converged, the desired output properties can be calculated [51].

4.7.5 CP2K

To perform DFT calculations in practice, a suitable software package must be selected. While accurate results can nowadays be achieved with a large number of different codes,

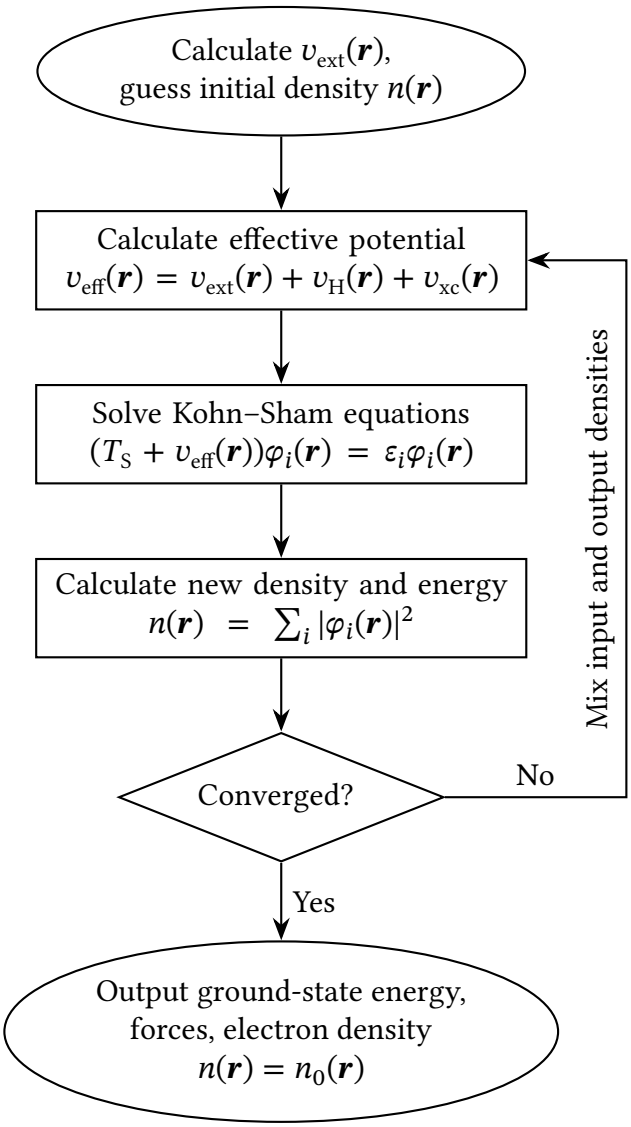

Figure 4.3: Self-consistency algorithm for DFT calculations

their computational details can vary significantly. An important aspect that needs to be considered is, for example, which types of simulations the program has been optimized for. Since this thesis primarily involves hybrid functional DFT calculations combined with the NEB method, both of which are computationally more demanding than standard LDA or GGA analyses, `CP2K` [64] was selected as a suitable software package. This code is optimized to reduce the computational effort required to evaluate the Hartree–Fock exchange contribution and supports the use of larger supercells. It employs a dual basis set approach, combining a primary set of Gaussian orbitals with an auxiliary plane-wave basis set [65].

The hybrid functional applied in this thesis is PBE0-TC-LR, a modified version of PBE0. More precisely, the standard PBE0 exchange energy can be expressed as

$$E_{\mathrm{x}}^{\mathrm{PBE0}} = \alpha E_{\mathrm{x}} + (1-\alpha) E_{\mathrm{x}}^{\mathrm{PBE}} \tag{4.27}$$

with α specifying the fraction of exact Hartree–Fock exchange E_{x}. However, evaluating this expression under periodic boundary conditions is challenging due to a singularity in the Coulombic Hartree–Fock interaction potential. To address this, truncating the interaction and setting it to 0 outside a cutoff radius r_c has become common practice [66]. Additionally, the missing description of the exchange contributions outside r_c is corrected to further improve the convergence behaviour. The truncation avoids the singularity in periodic systems, while the long-range correction ensures an accurate description of the exchange energy at larger distances, improving both physical accuracy and computational efficiency. This results in the long-range corrected truncated Coulomb exchange functional PBE0-TC-LRC, which requires significantly fewer computational resources to evaluate than the full PBE0 functional:

$$E_{\mathrm{x}}^{\mathrm{PBE0-TC-LRC}} = \alpha E_{\mathrm{x}}^{\mathrm{TC}} + \alpha E_{\mathrm{x}}^{\mathrm{PBE-LRC}} + (1-\alpha) E_{\mathrm{x}}^{\mathrm{PBE}}. \tag{4.28}$$

In this functional, the Hartree–Fock exchange energy is replaced by the truncated Coulomb term $E_{\mathrm{x}}^{\mathrm{TC}}$, and long-range corrections $E_{\mathrm{x}}^{\mathrm{PBE-LRC}}$ from the standard PBE method are added [67].

In hybrid DFT calculations using CP2K, evaluating the Hartree–Fock exchange energy is one of the most computationally demanding steps, particularly for large systems. To circumvent this limitation, the auxiliary density matrix method (ADMM) has been developed. It introduces an auxiliary basis set with a corresponding density matrix, chosen to be smaller than the primary basis set. This allows the Hartree–Fock exchange to be approximated with a significantly reduced number of terms, since it only needs to be calculated using the auxiliary density matrix rather than the full-sized one.

4.7.6 VASP

Additional calculations performed within the Vienna Ab initio Simulation Package (VASP) [68] allow for a comparison with the results obtained from CP2K and thus help to assess the convergence and precision. More importantly, since CP2K only takes the Γ-point into account when sampling the Brillouin zone, additional analyses using VASP also offer the possibility of studying the influence of different k-point grids. For example, this allows for a comparison between Brillouin zone sampling of only the Γ-point and a $2 \times 2 \times 2$ grid. In contrast to CP2K, VASP relies on a plane-wave basis set with the PAW method, which treats the periodic boundary conditions differently. Furthermore, Hartree–Fock exchange is implemented in reciprocal space, which is more efficient for

plane waves and avoids the divergence issues encountered by CP2K with Gaussian basis sets [69].

As a result, the implementation of the full PBE0 functional in VASP does not suffer from the same numerical instabilities as in CP2K. Moreover, the long-range part of the exchange is handled more naturally in reciprocal space, eliminating the need for truncation. In terms of computational efficiency, VASP's fast Fourier transform (FFT) based approach for Hartree–Fock exchange is optimized for plane waves, making standard PBE0 feasible even for large periodic systems [59, 70].

5

The Actors: Self-Trapped Excitons

5.1 Localization in Excited States

To understand how STEs can form and influence a material's properties, it is first necessary to explore how charge carriers interact with the lattice in solids. In condensed matter physics, quasiparticles are introduced to describe the collective behaviour of electrons and atoms. One such quasiparticle is the polaron, proposed by Landau [71] and Pekar [72] to explain an electron moving in a crystal where the surrounding atoms displace to screen its charge. This electron–phonon coupling increases the electron's effective mass, as if it were dragging the heavier ionic cores along with it, thus lowering its mobility. In large ionic crystals, where Coulomb interactions are strong, this effect is particularly pronounced [73]. In practical applications, polarons can significantly reduce electron mobility in semiconductors and influence the optical conductivity of photoactive materials [74]. Polarons are typically classified as large (delocalized, moving close to the band edge with slightly increased mass) or small (localized at a single ion, moving via hopping or tunnelling). The key idea is that charge carriers can localize due to lattice deformations [75]. This localization concept not only applies to single charges, but can also lead to the formation of double polarons (bound pairs of identical charge carriers, like O dimers), which further stabilize localized states [76]. When two oppositely charged polarons – an electron polaron and a hole polaron – interact, they can form a bound electron–hole pair, called an exciton. If the exciton's interaction with the lattice is strong enough, the entire electron–hole pair can become localized, collectively distorting the surrounding lattice. This localized, lattice-distorted state is the fundamental property of an STE. Unlike free excitons, which move through the crystal relatively easily, STEs are tied in place by their own lattice distortion, leading to unique optical and structural properties [75]. STEs are particularly prominent in materials where electron–phonon coupling is strong, such as alkali halides, perovskites,

and transition metal oxides. Their formation can alter optical properties (for example broad emission bands), affect charge transport, and even act as precursor to defect formation [77]. Understanding STEs is therefore essential for applications ranging from optoelectronics to photocatalysis. In the following sections, the mechanisms behind STE formation, their theoretical description, and their implications for material properties are discussed further.

5.2 Formation of Self-Trapped Excitons

In crystals, excitons interact with phonons (lattice vibrations), which leads to scattering if this electron–phonon coupling is weak. However, if the coupling is strong, it can lead to a localization of not only single charge carriers, but also the bound electron–hole pairs, to form an STE. This evolution from delocalized to localized states is illustrated in Fig. 5.1. Free, delocalized electrons and holes localize to form electron and hole polarons. When these polarons interact, they can trap each other and eventually form an STE. In the latter case, the entire electron–hole pair distorts the lattice, pinning itself in place [78]. This process demonstrates that STEs are a natural extension of polaron

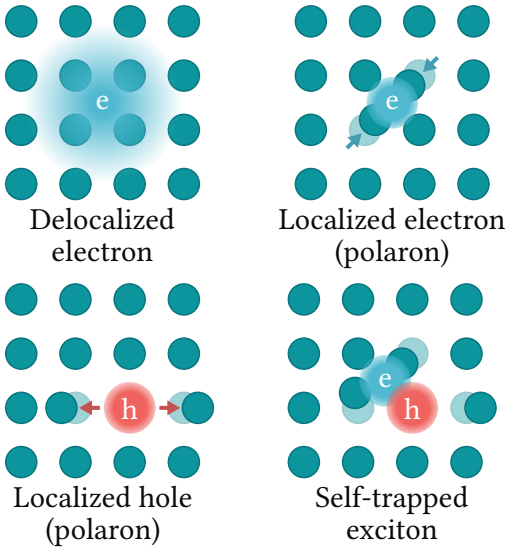

Figure 5.1: Schematic of charge localization in solids. A delocalized electron localizes to form an electron polaron. It interacts with a hole polaron to trap each other, and an STE is created.

physics, where the bound electron–hole pair collectively distorts the lattice to lower the total energy of the system. The kinetic cost of localizing the exciton is compensated for by the energy gain from the lattice relaxation, which lowers the potential energy and results in a net energy reduction [78].

The formation of an STE can also be visualized in a configurational coordinate diagram (see Fig. 5.2). In this representation, the energy of the system is plotted as a function of a generalized lattice distortion coordinate, for example a bond length or collective atomic displacement. The free exciton state, which is delocalized and therefore has a comparatively higher energy, corresponds to a wider and shallower potential well. In contrast, the STE induces a local lattice distortion and shifts the system to a deeper, narrow well with lower total energy [77]. The energy difference between the absorption (free exciton) and emission (STE) peaks is known as the Stokes shift, a characteristic feature of STEs that can also be observed experimentally as a red-shifted, broadened emission band. This shift occurs because the lattice relaxes after excitation, lowering the emission energy relative to the absorption energy [79, 80].

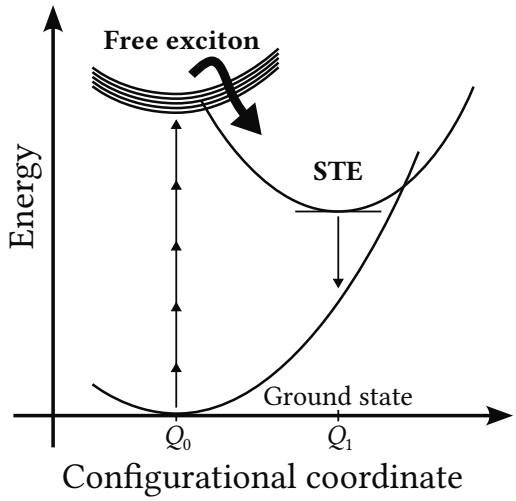

Figure 5.2: Configurational coordinate diagram illustrating the energy landscape of free excitons and STEs. The Stokes shift is the energy difference between the free exciton (absorption) and STE (emission) peaks.

The probability of STE formation is determined by two possible energy values. On the one hand, the formation energy describes the difference between the ground state of the pristine system and the excited, distorted lattice state (where the STE is present), which strongly depends on the material. On the other hand, the binding energy is obtained by comparing the self-trapped state (where the STE is present) with the state, where the two involved polarons are further apart and do not trap each other. Consequently, systems with weak electron–phonon coupling, where free excitons remain energetically favourable, typically do not exhibit STEs. In contrast, strong coupling, as commonly found in ionic crystals or mixed-metal oxides, can stabilize the STE as the lowest excited state of the system. To quantify this stabilization, the total energies of both configurations must be compared, including contributions from the electronic structure as well as the elastic energy associated with the lattice distortion [77].

5.3 Theoretical Description

An approach to the theoretical description of STEs is the use of simplified model Hamiltonians. Such an example is the Holstein Hamiltonian [81], which manages to describe the fundamentals of the self-trapping process by coupling the exciton to local phonon modes. The decision of whether the system can localize depends on the balance between the kinetic energy of the exciton and the potential energy gain from the lattice distortion. In materials with degenerate electronic states, such as transition metal oxides, lattice distortions can lift the degeneracy and lower the total energy, thereby stabilizing localized excitations, including STEs. This is called the Jahn–Teller effect [82].

To model STEs in realistic materials, two different approaches can typically be considered, each with certain consequences for the size of the simulation cell. The unit cell approach, in which the Hamiltonian is calculated for one single atomic cell, is generally viewed as computationally efficient for polarons, but becomes more expensive for STEs due to the need for combining it with the Bethe–Salpeter equation (BSE) to describe the excitonic states [83]. In this method, explicit large supercell calculations are avoided by expressing localized quasiparticles as coherent superpositions of Bloch-like electronic or excitonic states coupled to phonons. Within this framework, all relevant quantities, like band structures, excitonic states, and exciton–phonon coupling, are obtained from calculations in the primitive unit cell. Localizations then emerge via a self-consistent treatment of the coupling in reciprocal space. This way, a description of both localized and delocalized states becomes possible, without directly breaking the translational symmetry in real space [83, 84].

Meanwhile, the supercell approach, which involves adding charges to atomistic models containing tens to hundreds of atoms, is more straightforward from a theoretical point of view. In addition, it can allow for anharmonicity, migration, and interactions with defects and interfaces. Due to all these reasons, it is often preferred, despite its high computational cost, to investigate the STE behaviour and associated lattice distortions. This is achieved by applying DFT calculations, especially when combined with hybrid exchange–correlation functionals [85]. However, to obtain a more accurate description of excitonic states or optical excitations, approaches like time-dependent density functional theory (TD-DFT) or many-body perturbation theory based on the GW approximation and BSE (GW+BSE) can be employed to analyze the excited electronic configurations of STEs [86, 87]. The identification of STEs in simulations is usually based on localized charge densities, characteristic local lattice distortions, and energetic stabilization relative to delocalized excitonic configurations.

Despite these advances, the simulation of STEs remains a challenge. Particularly for the often required large supercells to properly describe localized excitons, accurate excited-state methods like TD-DFT or GW+BSE are computationally demanding. Furthermore, non-adiabatic effects can play a role in the charge transport via STEs or other carriers, requiring specialized approaches like non-adiabatic molecular dynamics. The

application of these techniques for complex materials, where STEs could interact or compete with defects, polarons, or other quasiparticles, is still under active research.

From the computational simulations, several key quantities for STE characterisation can be derived. The formation energy E_f describes the difference between the energy of the STE E_STE and the pristine system E_pristine and therefore provides information about the stability of the localized state. It is calculated according to

$$E_\mathrm{f} = E_\mathrm{STE} - E_\mathrm{pristine} + \epsilon_\mathrm{VBM} - \epsilon_\mathrm{CBM}, \tag{5.1}$$

where ϵ_VBM and ϵ_CBM describe the energies of the VBM and CBM in the pristine system, respectively. As a consequence, negative formation and binding energies thus indicate a thermodynamically favoured excited state. The energy barrier between the free exciton and STE, or between two different STE states, gives an additional estimate of the likelihood of a trapping or transitioning process happening. A high barrier suggests that thermal activation or non-adiabatic transitions might be needed, while a low or absent barrier promotes spontaneous localization. Finally, estimates for the timescale of STE formation after photoexcitation help understanding the dynamics and stability. These time delays can be calculated using the Arrhenius equation for the rate constant k of a thermally activated process

$$k = \kappa \nu \Gamma \exp\left(-\frac{E}{k_\mathrm{B} T}\right) \tag{5.2}$$

with the activation energy E, the Boltzmann constant k_B, the temperature T and the attempt frequency ν [88]. The electronic transmission coefficient κ is defined as

$$\kappa = \frac{2P}{1+P}. \tag{5.3}$$

In many cases, the adiabatic regime can be assumed, in which $P \to 1$, and thus $\kappa = 1$. Furthermore, the nuclear tunnelling factor Γ should only be important for low temperatures or light elements and can therefore also be set to 1 [74, 89]. The attempt frequency can be obtained from the second derivative of the energy with respect to the configurational coordinate at the polaron ground state Q_0:

$$\nu = \sqrt{\frac{\partial^2 E(Q)}{\partial Q^2}\Big|_{Q=Q_0}}, \tag{5.4}$$

with the configurational coordinate Q calculated as

$$Q_i = \sqrt{\sum_j m_j \left| r_{i,j} - r_{0,j} \right|^2}. \tag{5.5}$$

Here, i indexes the structure in the pathway, while m_j and $r_{i,j}$ are the mass and position of atom j [89]. The timescale τ is finally found with the inverse of the rate constant

$$\tau = \frac{1}{k}. \tag{5.6}$$

5.4 Properties and Implications

Having established the fundamentals of STEs, their intrinsic properties and broader implications can now be discussed. Due to their localized nature, which is promoted by strong electron–phonon interactions, STEs exhibit unique optical, structural and dynamic behaviour. From an optical point of view, STEs show broad, red-shifted emission paths, a direct consequence of the large Stokes shift previously mentioned in Sect. 5.2. This shift, created by lattice relaxation, is a key experimental signature of STEs in photoluminescence spectra. In terms of structural characteristics, localized lattice distortions around the electron–hole pair are induced, which can lead to symmetric breathing modes or asymmetric (Jahn–Teller-like) distortions. The short-range nature of the electron–phonon coupling responsible for STE formation is reflected in these distortions [77]. The dynamics of the formation and dissociation processes typically show ultrafast timescales in the range of femto- to picoseconds. After photoexcitation, the system rapidly relaxes through lattice optimization to localize the exciton and create the STE configuration [90]. Subsequently, radiative recombination or dissociation into free carriers can occur. The rates of these processes are highly dependent on the electronic structure of the specific material and the phonon coupling strength [77, 91].

These unique properties of STEs have an important influence on the excited-state behaviour in a material. Due to their tendency to localize, STEs can act as temporary traps that potentially lead to an impeded carrier mobility, and therefore alter the overall charge transport processes. Furthermore, if no rapid dissociation takes place, the prolonged localization may serve as a precursor to defect formation, possibly leading to permanent structural changes [91, 92]. In photoactive materials, the large Stokes shift and broad emission bands can lead to contrasting influences. On one hand, applications in optoelectronics might be enabled, on the other hand, it can indicate energy losses in photovoltaics. Which effect is prevalent in the end is determined by the competition between recombination and dissociation pathways [80, 93]. Therefore, understanding these properties is essential for interpreting the behaviour of excited states in both experimental and computational studies.

5.5 Open Questions and Challenges

Although significant progress in understanding STEs has been made in recent times, there are still theoretical and experimental challenges. Computationally, treating coupled dynamics of excited states and lattice distortions accurately in complex materials like hybrid perovskites or transition metal oxides remains demanding, especially for large supercells or non-adiabatic processes. Open questions are, among others, under which conditions STEs form rather than free excitons or polarons, and how STEs interact with defects, interfaces, or other quasiparticles in realistic systems.

6

The Story: Summary of Papers

Paper I

Competing Self-Trapped Exciton States and Multiple Emission Pathways in $BiVO_4$

In **Paper I**, the formation of STEs in $BiVO_4$ is studied. A search for localized exciton configurations is carried out using hybrid functional DFT computations. The found STE structures are then investigated regarding their formation and emission energies as well as their localization, stability, and optical properties. Furthermore, the convergence of energies with the size of the simulation cell is tested.

We find that two distinct STE types can form in $BiVO_4$, one that is extended over several atoms (STE1), and one compact, located in proximity of two neighbouring atoms (STE2). Both configurations, however, exhibit comparable formation energies, suggesting that both types of STE could potentially exist at the same time, leading to interesting interactions and transformations. Moreover, we investigate the emission energies and show that emission from a single STE configuration leads to multiple peaks in the emission spectrum due to different types of internal transitions. Upon comparison with experimental studies, our results show good agreement with measured emission peaks. In addition, we show that although STEs are neutral, the results are sensitive to the applied cell size.

Paper II

Evolution of Excited States in Bismuth Vanadate: Trapping and Kinetic Pathways

In **Paper II**, the study of the two types of STEs found in $BiVO_4$ is continued to investigate their trapping and kinetics. Different pathways for trapping, transformation, and hopping of STEs are identified and analyzed using NEB calculations. The energy barriers give an estimate for the probability of a certain process taking place. In addition, the time scales on which these processes can occur are approximated to allow for a comparison with experimental measurements.

Our investigations show that one of the STE configurations is much more mobile than the other, since it can separate more easily during the process. However, this also leads to the STE dissociating rather than participating in any other hopping or transition. The second type of STE appears to be more rigid, with larger barriers for hopping, dissociation, and transformation, meaning that going from STE1 to STE2 is easier than the other way around. To also consider processes that would occur with longer time delays, we study the trapping of charges within O–O hole dimers. This formation provides alternative pathways with much higher energy barriers.

To put our results in context, we calculate the time delays that the investigated processes would take place with, and compare them to experimental transient absorption spectra. We find that the STE processes occur in the sub-picosecond to nanosecond range, while the dimer processes take longer, with times on the scale of nanoseconds to even microseconds. These order-of-magnitude estimates agree well with the emission time delays of experimental references.

7

The Future: Outlook

This thesis presents studies on the formation, stability, and mobility of STEs in bulk $BiVO_4$, providing fundamental insights into charge localization mechanisms in this material. The work includes hybrid functional DFT calculations to identify two distinct STE configurations with comparable formation energies and emission spectra that match experimental data. In addition, the energies are shown to be sensitive to the simulation cell size. Furthermore, NEB calculations are applied to investigate STE trapping, transformation, and hopping, revealing differing mobilities and time scales (subpicosecond to microsecond) that align with experimental transient absorption spectra.

While these results contribute to a deeper understanding of the electronic properties of $BiVO_4$, the key processes governing PEC water splitting occur at the semiconductor surface and within the near-surface region, which have not been investigated in this work. Extending the present first-principles studies to surfaces and subsurface layers is therefore a natural next step towards elucidating the mechanisms controlling charge separation, transport, and recombination during the OER and HER. In particular, simulations of STEs in surfaces with different crystallographic orientations could reveal how the surface structure influences charge localization and stability through changes in formation energies and migration barriers. Such investigations would not only provide insights into favourable surface configurations for efficient charge carrier dynamics but also guide designs towards a more effective photocatalyst for the water splitting reaction.

Since the relative stabilities of localized charges are shown to be sensitive to computational setup and technique, a systematic comparison of electronic structure methods would be of interest. In particular, investigating the dependence of STE stability on the construction and parametrization of hybrid exchange–correlation functionals across a wider range of materials could provide valuable findings to improve simulation approaches.

The methodologies employed here could also be extended to other photocatalytic materials, where excitonic charge localization remains comparatively unexplored. Studies across different semiconductor families may improve the understanding of the factors governing self-trapping and its influence on photocatalytic performance and act as a benchmark for future research work.

Furthermore, recent advances in machine-learning models for polarons at semiconductor interfaces suggest a promising route towards studying STEs in a more realistic environment, for example in the vicinity of water and at finite temperatures. This approach is being applied in ongoing work, focusing on the stability of polarons and oxygen vacancies at the $BiVO_4$–water interface, where machine-learning-driven simulations can reveal how free energies, transition levels, and charge trapping evolve under operando conditions. Combined with ongoing first-principles studies of STEs localized near the surface, developments like these may ultimately enable large-scale simulations of STE formation, transport, and recombination under realistic photocatalytic operating conditions.

Acknowledgments

The work presented in this thesis could not have been carried out without the contributions and guidance of many people. I especially thank my supervisor Julia Wiktor for her constant support, invaluable advice, and unlimited readiness to answer any question at (almost) every time of the day. I am also grateful to my examiner Henrik Grönbeck for his valuable feedback and guidance, which helped shape my journey. Additionally, many thanks to all my colleagues for always being open to discussions and contributing to creating a friendly atmosphere and fun working environment.

Furthermore, I would like to thank my parents for their endless support and interest in my work, as well as Emma for always being there for me and happy to discuss any topic that comes to mind. Lastly, I of course also want to say thank you to my friends, in particular Moritz, and family for always backing my ideas and plans, even when the time for meeting in person is sometimes very limited.

Bibliography

[1] C. Méndez-Vallejo, N. Simpson, F. Johnson, and A. Birt, *Climate Change 2023: Synthesis Report. Contribution of Working Groups I, II and III to the Sixth Assessment Report of the Intergovernmental Panel on Climate Change* (IPCC, Geneva, Switzerland., 2023). doi:10.59327/IPCC/AR6-9789291691647.

[2] X. Lan, P. Tans, K. Thoning, and N. G. M. Laboratory, *Trends in globally-averaged CO_2 determined from NOAA Global Monitoring Laboratory measurements,* NOAA GML, 2026. doi:10.15138/9N0H-ZH07.

[3] K. Thoning, E. Dlugokencky, X. Lan, and N. G. M. Laboratory, *Trends in globally-averaged CH_4, N_2O, and SF_6,* NOAA GML, 2026. doi:10.15138/P8XG-AA10.

[4] H. Ritchie, M. Roser, and P. Rosado, *Renewable Energy,* Our World in Data, 2020. https://ourworldindata.org/renewable-energy.

[5] M. Yue, H. Lambert, E. Pahon, R. Roche, S. Jemei, and D. Hissel, *Hydrogen energy systems: A critical review of technologies, applications, trends and challenges,* Renewable and Sustainable Energy Reviews **146**, 111180 (2021). doi:10.1016/j.rser.2021.111180.

[6] J. Rosenow and R. Lowes, *Will blue hydrogen lock us into fossil fuels forever?,* One Earth **4**, 1527 (2021). doi:10.1016/j.oneear.2021.10.018.

[7] N. S. Lewis and D. G. Nocera, *Powering the planet: Chemical challenges in solar energy utilization,* Proceedings of the National Academy of Sciences **103**, 15729 (2006). doi:10.1073/pnas.0603395103.

[8] J. A. Turner, *Sustainable Hydrogen Production,* Science **305**, 972 (2004). doi:10.1126/science.1103197.

[9] H. M. Chen, C. K. Chen, R.-S. Liu, L. Zhang, J. Zhang, and D. P. Wilkinson, *Nano-architecture and material designs for water splitting photoelectrodes,* Chem. Soc. Rev. **41**, 5654 (2012). doi:10.1039/C2CS35019J.

[10] J. K. Nørskov, J. Rossmeisl, A. Logadottir, L. Lindqvist, J. R. Kitchin, T. Bligaard, and H. Jónsson, *Origin of the Overpotential for Oxygen Reduction at a Fuel-Cell Cathode,* The Journal of Physical Chemistry B **108**, 17886 (2004). PMID: 39682080. doi:10.1021/jp047349j.

[11] E. Fabbri and T. J. Schmidt, *Oxygen Evolution Reaction—The Enigma in Water Electrolysis,* ACS Catalysis **8**, 9765 (2018). doi:10.1021/acscatal.8b02712.

[12] A. Fujishima and K. Honda, *Electrochemical Photolysis of Water at a Semiconductor Electrode,* Nature **238**, 37 (1972). doi:10.1038/238037a0.

[13] J. Rossmeisl, A. Logadottir, and J. Nørskov, *Electrolysis of water on (oxidized) metal surfaces,* Chemical Physics **319**, 178 (2005). Molecular Charge Transfer in Condensed Media - from Physics and Chemistry to Biology and Nanoengineering in honour of Alexander M. Kuznetsov on his 65th birthday. doi:10.1016/j.chemphys.2005.05.038.

[14] K. Zeng and D. Zhang, *Recent progress in alkaline water electrolysis for hydrogen production and applications,* Progress in Energy and Combustion Science **36**, 307 (2010). doi:10.1016/j.pecs.2009.11.002.

[15] I. Chorkendorff and J. Niemantsverdriet, *Concepts of Modern Catalysis and Kinetics* (John Wiley & Sons, Ltd, 2017). ISBN 9783527332687.

[16] A. Bard and L. Faulkner, *Electrochemical Methods: Fundamentals and Applications* (John Wiley & Sons, Ltd, 2000). ISBN 9780471043720.

[17] E. M. Stuve, *Overpotentials in Electrochemical Cells.* In G. Kreysa, K.-i. Ota, and R. F. Savinell, eds., *Encyclopedia of Applied Electrochemistry* (New York, NY: Springer New York, 2014). doi:10.1007/978-1-4419-6996-5_330.

[18] M. G. Walter, E. L. Warren, J. R. McKone, S. W. Boettcher, Q. Mi, E. A. Santori, and N. S. Lewis, *Solar Water Splitting Cells,* Chemical Reviews **110**, 6446 (2010). PMID: 21062097. doi:10.1021/cr1002326.

[19] T. Hisatomi, J. Kubota, and K. Domen, *Recent advances in semiconductors for photocatalytic and photoelectrochemical water splitting,* Chem. Soc. Rev. **43**, 7520 (2014). doi:10.1039/C3CS60378D.

[20] Y. Park, K. J. McDonald, and K.-S. Choi, *Progress in bismuth vanadate photoanodes for use in solar water oxidation,* Chem. Soc. Rev. **42**, 2321 (2013). doi:10.1039/C2CS35260E.

[21] H. L. Tan, R. Amal, and Y. H. Ng, *Alternative strategies in improving the photocatalytic and photoelectrochemical activities of visible light-driven $BiVO_4$: a review,* J. Mater. Chem. A **5**, 16498 (2017). doi:10.1039/C7TA04441K.

[22] M. Ni, M. K. Leung, D. Y. Leung, and K. Sumathy, *A review and recent developments in photocatalytic water-splitting using TiO_2 for hydrogen production,* Renewable and Sustainable Energy Reviews **11**, 401 (2007). doi:10.1016/j.rser.2005.01.009.

[23] M. Ismael, *A review and recent advances in solar-to-hydrogen energy conversion based on photocatalytic water splitting over doped-TiO_2 nanoparticles,* Solar Energy **211**, 522 (2020). doi:10.1016/j.solener.2020.09.073.

[24] P. E. de Jongh, D. Vanmaekelbergh, and J. J. Kelly, *Photoelectrochemistry of Electrodeposited Cu_2O,* Journal of The Electrochemical Society **147**, 486 (2000). doi:10.1149/1.1393221.

[25] L. Wu, L.-k. Tsui, N. Swami, and G. Zangari, *Photoelectrochemical Stability of Electrodeposited Cu_2O Films,* The Journal of Physical Chemistry C **114**, 11551 (2010). doi:10.1021/jp103437y.

[26] Q. Campbell and I. Dabo, *Electrochemical stability and light-harvesting ability of silicon photoelectrodes in aqueous environments,* The Journal of Chemical Physics **151**, 044109 (2019). doi:10.1063/1.5093810.

[27] D. Arumugam, J. P. Sivakumar, A. Muralidharan, and S. Ramasamy, *Exploring the electrocatalytic performance of silicene and single atom doped silicene for HER, OER and ORR*

activity using density functional theory, Chemical Physics Impact **9**, 100664 (2024). doi:10.1016/j.chphi.2024.100664.

[28] K. T. Fountaine, H. J. Lewerenz, and H. A. Atwater, *Efficiency limits for photoelectrochemical water-splitting,* Nature Communications **7**, 13706 (2016). doi:10.1038/ncomms13706.

[29] B. A. Pinaud, J. D. Benck, L. C. Seitz, A. J. Forman, Z. Chen, T. G. Deutsch, B. D. James, K. N. Baum, G. N. Baum, S. Ardo, H. Wang, E. Miller, and T. F. Jaramillo, *Technical and economic feasibility of centralized facilities for solar hydrogen production via photocatalysis and photoelectrochemistry,* Energy Environ. Sci. **6**, 1983 (2013). doi:10.1039/C3EE40831K.

[30] A. Kudo, K. Omori, and H. Kato, *A Novel Aqueous Process for Preparation of Crystal Form-Controlled and Highly Crystalline $BiVO_4$ Powder from Layered Vanadates at Room Temperature and Its Photocatalytic and Photophysical Properties,* Journal of the American Chemical Society **121**, 11459 (1999). doi:10.1021/ja992541y.

[31] A. Sleight, H. y. Chen, A. Ferretti, and D. Cox, *Crystal growth and structure of $BiVO_4$,* Materials Research Bulletin **14**, 1571 (1979). doi:10.1016/0025-5408(72)90227-9.

[32] A. J. E. Rettie, W. D. Chemelewski, J. Lindemuth, J. S. McCloy, L. G. Marshall, J. Zhou, D. Emin, and C. B. Mullins, *Anisotropic small-polaron hopping in W:$BiVO_4$ single crystals,* Applied Physics Letters **106**, 022106 (2015). doi:10.1063/1.4905786.

[33] H. Wu, L. Zhang, S. Qu, A. Du, J. Tang, and Y. H. Ng, *Polaron-Mediated Transport in $BiVO_4$ Photoanodes for Solar Water Oxidation,* ACS Energy Letters **8**, 2177 (2023). doi:10.1021/acsenergylett.3c00465.

[34] J. Bierlein and A. Sleight, *Ferroelasticity in $BiVO_4$,* Solid State Communications **16**, 69 (1975). doi:10.1016/0038-1098(75)90791-7.

[35] T. Liu, X. Zhang, J. Guan, C. R. A. Catlow, A. Walsh, A. A. Sokol, and J. Buckeridge, *Insight into the Fergusonite–Scheelite Phase Transition of ABO_4-Type Oxides by Density Functional Theory: A Case Study of the Subtleties of the Ground State of $BiVO_4$,* Chemistry of Materials **34**, 5334 (2022). doi:10.1021/acs.chemmater.1c04417.

[36] P. Schwinghammer, F. S. Hegner, F. P. Delgado, M. Panhans, K. Merkel, F. Ortmann, I. D. Sharp, and D. A. Egger, *Interplay between Electronic Structure, Chemical Bonding, and Lattice Symmetry in Bismuth Vanadate,* 2026. doi:10.48550/arXiv.2607.08327.

[37] S. Tokunaga, H. Kato, and A. Kudo, *Selective Preparation of Monoclinic and Tetragonal $BiVO_4$ with Scheelite Structure and Their Photocatalytic Properties,* Chemistry of Materials **13**, 4624 (2001). doi:10.1021/cm0103390.

[38] H. Seo, Y. Ping, and G. Galli, *Role of Point Defects in Enhancing the Conductivity of $BiVO_4$,* Chemistry of Materials **30**, 7793 (2018). doi:10.1021/acs.chemmater.8b03201.

[39] F. Wu and Y. Ping, *Combining Landau–Zener theory and kinetic Monte Carlo sampling for small polaron mobility of doped $BiVO_4$ from first-principles,* Journal of Materials Chemistry A **6**, 20025 (2018). doi:10.1039/c8ta07437b.

[40] A. J. E. Rettie, H. C. Lee, L. G. Marshall, J.-F. Lin, C. Capan, J. Lindemuth, J. S. McCloy, J. Zhou, A. J. Bard, and C. B. Mullins, *Combined Charge Carrier Transport and Photoelectrochemical Characterization of $BiVO_4$ Single Crystals: Intrinsic Behavior of a Complex Metal Oxide,* Journal of the American Chemical Society **135**, 11389 (2013). PMID: 23869474. doi:10.1021/ja405550k.

[41] J. R. Bolton, S. J. Strickler, and J. S. Connolly, *Limiting and realizable efficiencies of solar photolysis of water,* Nature **316**, 495 (1985). doi:10.1038/316495a0.

[42] G. S. Kamble, T. S. Natarajan, S. S. Patil, M. Thomas, R. K. Chougale, P. D. Sanadi, U. S. Siddharth, and Y.-C. Ling, *$BiVO_4$ As a Sustainable and Emerging Photocatalyst: Synthesis Methodologies, Engineering Properties, and Its Volatile Organic Compounds Degradation Efficiency,* Nanomaterials **13**, (2023). doi:10.3390/nano13091528.

[43] J. Zhang, J. Shi, Y. Chen, K. H. L. Zhang, and Y. Yang, *Bimolecular Self-Trapped Exciton Formation in Bismuth Vanadate,* The Journal of Physical Chemistry Letters **13**, 9815 (2022). PMID: 36228113. doi:10.1021/acs.jpclett.2c02596.

[44] J. Ravensbergen, F. F. Abdi, J. H. van Santen, R. N. Frese, B. Dam, R. van de Krol, and J. T. M. Kennis, *Unraveling the Carrier Dynamics of $BiVO_4$: A Femtosecond to Microsecond Transient Absorption Study,* The Journal of Physical Chemistry C **118**, 27793 (2014). doi:10.1021/jp509930s.

[45] E. N. Fernandez, D. A. Grave, R. van de Krol, and F. F. Abdi, *Strain-Induced Distortions Modulate the Optoelectronic Properties of Epitaxial $BiVO_4$ Films,* Advanced Energy Materials **13**, 2301075 (2023). doi:10.1002/aenm.202301075.

[46] A. Bhattacharya, K. Mallick, and A. Hartridge, *Phase transition in $BiVO_4$,* Materials Letters **30**, 7 (1997). doi:10.1016/S0167-577X(96)00162-0.

[47] I. Laraib, M. A. Carneiro, and A. Janotti, *Effects of Doping on the Crystal Structure of $BiVO_4$,* The Journal of Physical Chemistry C **123**, 26752 (2019). doi:10.1021/acs.jpcc.9b05858.

[48] E. N. Fernandez, R. van de Krol, and F. F. Abdi, *Tuning the Optical and Photoelectrochemical Properties of Epitaxial $BiVO_4$ by Lattice Strain,* Small Structures **5**, 2400097 (2024). doi:10.1002/sstr.202400097.

[49] A. Szabo and N. Ostlund, *Modern Quantum Chemistry: Introduction to Advanced Electronic Structure Theory* (Dover Publications, 1996). ISBN 9780486691862.

[50] M. Born and R. Oppenheimer, *Zur Quantentheorie der Molekeln,* Annalen der Physik **389**, 457 (1927). doi:10.1002/andp.19273892002.

[51] P. Puschnig, *Fundamentals of Electronic Structure Theory,* 2022.

[52] P. Hohenberg and W. Kohn, *Inhomogeneous Electron Gas,* Phys. Rev. **136**, B864 (1964). doi:10.1103/PhysRev.136.B864.

[53] W. Kohn and L. J. Sham, *Self-Consistent Equations Including Exchange and Correlation Effects,* Phys. Rev. **140**, A1133 (1965). doi:10.1103/PhysRev.140.A1133.

[54] J. P. Perdew and K. Burke, *Comparison shopping for a gradient-corrected density functional,* International Journal of Quantum Chemistry **57**, 309 (1996). doi:10.1002/(SICI)1097-461X(1996)57:3<309::AID-QUA4>3.0.CO;2-1.

[55] C. Fiolhais, F. Nogueira, and M. A. Marques, *A primer in density functional theory* (Springer Science & Business Media, 2003). ISBN 9783540030836. doi:10.1007/3-540-37072-2.

[56] J. P. Perdew, K. Burke, and M. Ernzerhof, *Generalized Gradient Approximation Made Simple,* Phys. Rev. Lett. **77**, 3865 (1996). doi:10.1103/PhysRevLett.77.3865.

[57] J. P. Perdew, M. Ernzerhof, and K. Burke, *Rationale for mixing exact exchange with density functional approximations,* The Journal of Chemical Physics **105**, 9982 (1996). doi:10.1063/1.472933.

[58] A. D. Becke, *A new mixing of Hartree–Fock and local density-functional theories,* The Journal of Chemical Physics **98**, 1372 (1993). doi:10.1063/1.464304.

[59] J. Paier, M. Marsman, K. Hummer, G. Kresse, I. C. Gerber, and J. G. Ángyán, *Screened hybrid density functionals applied to solids,* The Journal of Chemical Physics **124**, 154709 (2006). doi:10.1063/1.2187006.

[60] G. Henkelman, B. P. Uberuaga, and H. Jónsson, *A climbing image nudged elastic band method for finding saddle points and minimum energy paths,* The Journal of Chemical Physics **113**, 9901 (2000). doi:10.1063/1.1329672.

[61] F. Bloch, *Über die Quantenmechanik der Elektronen in Kristallgittern,* Zeitschrift für Physik **52**, 555 (1929). doi:10.1007/BF01339455.

[62] P. W. Atkins and R. S. Friedman, *Molecular Quantum Mechanics* (Oxford University Press, 2011). ISBN 9780199541423.

[63] P. E. Blöchl, *Projector augmented-wave method,* Phys. Rev. B **50**, 17953 (1994). doi:10.1103/PhysRevB.50.17953.

[64] T. D. Kühne, M. Iannuzzi, M. Del Ben, V. V. Rybkin, P. Seewald, F. Stein, T. Laino, R. Z. Khaliullin, O. Schütt, F. Schiffmann, D. Golze, J. Wilhelm, S. Chulkov, M. H. Bani-Hashemian, V. Weber, U. Borštnik, M. Taillefumier, A. S. Jakobovits, A. Lazzaro, H. Pabst, T. Müller, R. Schade, M. Guidon, S. Andermatt, N. Holmberg, G. K. Schenter, A. Hehn, A. Bussy, F. Belleflamme, G. Tabacchi, A. Glöß, M. Lass, I. Bethune, C. J. Mundy, C. Plessl, M. Watkins, J. VandeVondele, M. Krack, and J. Hutter, *CP2K: An electronic structure and molecular dynamics software package - Quickstep: Efficient and accurate electronic structure calculations,* The Journal of Chemical Physics **152**, 194103 (2020). doi:10.1063/5.0007045.

[65] G. Lippert, J. Hutter, and M. Parrinello, *A hybrid Gaussian and plane wave density functional scheme,* Molecular Physics **92**, 477 (1997). doi:10.1080/002689797170220.

[66] J. Spencer and A. Alavi, *Efficient calculation of the exact exchange energy in periodic systems using a truncated Coulomb potential,* Phys. Rev. B 77, 193110 (2008). doi:10.1103/PhysRevB.77.193110.

[67] M. Guidon, J. Hutter, and J. VandeVondele, *Robust Periodic Hartree–Fock Exchange for Large-Scale Simulations Using Gaussian Basis Sets,* Journal of Chemical Theory and Computation **5**, 3010 (2009). PMID: 26609981. doi:10.1021/ct900494g.

[68] J. Hafner and G. Kresse, *The Vienna AB-Initio Simulation Program VASP: An Efficient and Versatile Tool for Studying the Structural, Dynamic, and Electronic Properties of Materials.* In A. Gonis, A. Meike, and P. E. A. Turchi, eds., *Properties of Complex Inorganic Solids* (Boston, MA: Springer US, 1997). doi:10.1007/978-1-4615-5943-6_10.

[69] G. Kresse and J. Furthmüller, *Efficiency of ab-initio total energy calculations for metals and semiconductors using a plane-wave basis set,* Computational Materials Science **6**, 15 (1996). doi:10.1016/0927-0256(96)00008-0.

[70] J. Heyd, G. E. Scuseria, and M. Ernzerhof, *Hybrid functionals based on a screened Coulomb potential,* The Journal of Chemical Physics **118**, 8207 (2003). doi:10.1063/1.1564060.

[71] L. D. Landau, *Electron motion in crystal lattices,* Phys. Z. Sowjet. **3**, 664 (1933).

[72] S. Pekar, *Autolocalization of the electron in an inertially polarizable dielectric medium,* Zh. Eksp. Teor. Fiz **16**, 043059 (1946).

[73] H. Fröhlich, *Electrons in lattice fields,* Advances in Physics **3**, 325 (1954). doi:10.1080/00018735400101213.

[74] D. Emin and T. Holstein, *Studies of small-polaron motion IV. Adiabatic theory of the Hall effect,* Annals of Physics **53**, 439 (1969). doi:10.1016/0003-4916(69)90034-7.

[75] C. Kittel, *Introduction to Solid State Physics* (Wiley, 2004). ISBN 9780471415268.

[76] A. M. Stoneham, *Theory of Defects in Solids: Electronic Structure of Defects in Insulators and Semiconductors* (Oxford University Press, 2001). ISBN 9780198507802. doi:10.1093/acprof:oso/9780198507802.001.0001.

[77] K. Song, Y. Toyozawa, and R. Williams, *Self-Trapped Excitons* (Springer Berlin Heidelberg, 1996). ISBN 9783540604464.

[78] Y. Toyozawa, *Self-Trapping of an Electron by the Acoustical Mode of Lattice Vibration. I:,* Progress of Theoretical Physics **26**, 29 (1961). doi:10.1143/PTP.26.29.

[79] R. T. Williams and M. N. Kabler, *Excited-state absorption spectroscopy of self-trapped excitons in alkali halides,* Phys. Rev. B **9**, 1897 (1974). doi:10.1103/PhysRevB.9.1897.

[80] J. Tan, D. Li, J. Zhu, N. Han, Y. Gong, and Y. Zhang, *Self-trapped excitons in soft semiconductors,* Nanoscale **14**, 16394 (2022). doi:10.1039/D2NR03935D.

[81] T. Holstein, *Studies of polaron motion: Part I. The molecular-crystal model,* Annals of Physics **8**, 325 (1959). doi:https://doi.org/10.1016/0003-4916(59)90002-8.

[82] H. A. Jahn and E. Teller, *Stability of polyatomic molecules in degenerate electronic states - I—Orbital degeneracy,* Proceedings of the Royal Society of London. A. Mathematical and Physical Sciences **161**, 220 (1937). doi:10.1098/rspa.1937.0142.

[83] Z. Dai, C. Lian, J. Lafuente-Bartolome, and F. Giustino, *Excitonic Polarons and Self-Trapped Excitons from First-Principles Exciton-Phonon Couplings,* Phys. Rev. Lett. **132**, 036902 (2024). doi:10.1103/PhysRevLett.132.036902.

[84] W. H. Sio, C. Verdi, S. Poncé, and F. Giustino, *Polarons from First Principles, without Supercells,* Phys. Rev. Lett. **122**, 246403 (2019). doi:10.1103/PhysRevLett.122.246403.

[85] F. Mauri and R. Car, *First-Principles Study of Excitonic Self-Trapping in Diamond,* Phys. Rev. Lett. **75**, 3166 (1995). doi:10.1103/PhysRevLett.75.3166.

[86] M. S. Hybertsen and S. G. Louie, *Electron correlation in semiconductors and insulators: Band gaps and quasiparticle energies,* Phys. Rev. B **34**, 5390 (1986). doi:10.1103/PhysRevB.34.5390.

[87] G. Onida, L. Reining, and A. Rubio, *Electronic excitations: density-functional versus many-body Green's-function approaches,* Rev. Mod. Phys. **74**, 601 (2002). doi:10.1103/RevModPhys.74.601.

[88] R. A. Marcus, *Electron transfer reactions in chemistry. Theory and experiment,* Rev. Mod. Phys. **65**, 599 (1993). doi:10.1103/RevModPhys.65.599.

[89] G. Palermo, S. Falletta, and A. Pasquarello, *Migration of hole polarons in anatase and rutile TiO_2 through piecewise-linear functionals,* Phys. Rev. B **110**, 235205 (2024). doi:10.1103/PhysRevB.110.235205.

[90] K. Miyata, T. L. Atallah, and X.-Y. Zhu, *Lead halide perovskites: Crystal-liquid duality, phonon glass electron crystals, and large polaron formation,* Science Advances **3**, e1701469 (2017). doi:10.1126/sciadv.1701469.

[91] D. Emin, *Polarons* (Cambridge University Press, 2012). ISBN 9781139023436. doi:10.1017/CBO9781139023436.

[92] N. Itoh and M. Stoneham, *Materials Modification by Electronic Excitation* (Cambridge University Press, 2000). ISBN 9780511541254. doi:10.1017/CBO9780511541254.

[93] A. Wright, C. Verdi, R. Milot, G. Eperon, M. A. Pérez Osorio, H. Snaith, F. Giustino, M. Johnston, and L. Herz, *Electron–phonon coupling in hybrid lead halide perovskites,* Nature Communications **7**, 11755 (2016). doi:10.1038/ncomms11755.